Supplementary information: Direct-bonded diamond membranes for heterogeneous quantum and electronic technologies

Xinghan Guo[1], Mouzhe Xie[1,2,†], Anchita Addhya[1,†], Avery Linder[1,†], Uri Zvi [1], Stella Wang[3], Xiaofei Yu[3], Tanvi D. Deshmukh[3], Yuzi Liu[4], Ian N. Hammock[1], Zixi Li[1], Clayton T. DeVault[1,5], Amy Butcher[1], Aaron P. Esser-Kahn[1], David D. Awschalom[1,3,5], Nazar Delegan[1,5], Peter C. Maurer[1,5], F. Joseph Heremans[1,5], Alexander A. High[1,5,*]

[1]*Pritzker School of Molecular Engineering, University of Chicago, Chicago, IL 60637, USA*

[2]*School of Molecular Sciences, Arizona State University, Tempe, AZ 85287, USA*

[3]*Department of Physics, University of Chicago, Chicago, IL 60637, USA*

[4]*Center for Nanoscale Materials, Argonne National Laboratory, Lemont, IL 60439, USA*

[5]*Center for Molecular Engineering and Materials Science Division, Argonne National Laboratory, Lemont, IL 60439, USA*

[†] *These authors contributed equally to this work.*

[*]*E-mail: ahigh@uchicago.edu*

1 Fabrication process of membrane heterostructures

1.1 Diamond membrane synthesis and patterning

The diamond membrane synthesis follows the same method as described in our previous work.[1] The membrane tether layer was created via He^+ implantation (dose $5 \times 10^{16}\,\mathrm{cm}^{-2}$, energy $150\,\mathrm{keV}$), followed by multi-step annealing ($400\,^\circ\mathrm{C}$ for $8\,\mathrm{h}$, $800\,^\circ\mathrm{C}$ for $8\,\mathrm{h}$, and $1200\,^\circ\mathrm{C}$ for $2\,\mathrm{h}$) in a forming gas ($4\,\%$ H_2, $96\,\%$ Ar) environment. Membrane overgrowth was performed in a microwave plasma chemical vapor deposition (MPCVD) chamber at Argonne National Laboratory. Four membrane substrates discussed in this work have overgrown layers of $185\,\mathrm{nm}$, $260\,\mathrm{nm}$, $400\,\mathrm{nm}$ and $660\,\mathrm{nm}$, respectively. Overgrown substrates received either ion implantation (Si^+, Ge^+, Sn^+ or N^+) or δ-doping ^{15}N for color center creation. Substrates were then patterned and inductively coupled plasma (ICP)-etched to individual $200\,\mu\mathrm{m}$ by $200\,\mu\mathrm{m}$ membranes. In preparation of the pick-up step, membranes were undercut from substrates via electrochemical (EC) etching in fresh de-ionized water, leaving the membranes solely attached to the substrates by a small, breakable tether.

1.2 Membrane pick-up and transfer via patterned PDMS stamps

PDMS stamps were prepared by applying freshly mixed PDMS base and curing agent (Sylgard 184, Dow Corning) to a $4\,\mathrm{inch}$ silicon wafer with lithographically defined SU-8 (3050, $\approx 55\,\mu\mathrm{m}$ thick post baking) structures. Over 200 PDMS stamps with two different shapes can be generated on a single wafer. The PDMS1-stamp consists of four little square-shaped contacting fingers with $70\,\mu\mathrm{m}$ spacing, in order to break the diamond tether and pick up the membrane. The PDMS2-stamp contains a single large square with $300\,\mu\mathrm{m}$ length to flip and place the membrane. The membrane pick-up, flipping, and placement were carried out on a probe station (Signatone S1160). Schematics and microscope images of this process are shown in Figure S1 (a)-(d). In this work, we placed our membrane onto a resist-coated, pre-patterned fused silica substrate referred as intermediate wafer, as discussed in section 1.3. Beyond this work, the patterned PDMS stamps can also be applied to HSQ-based membrane placements[1] to improve the device yield.

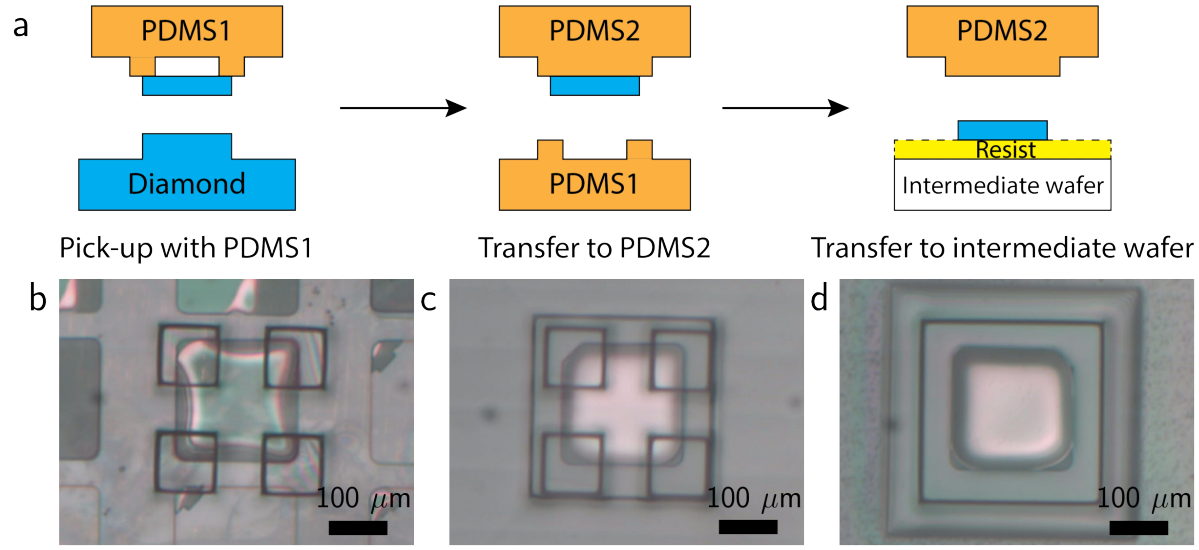

Figure S1: Deterministic diamond membrane transfer via patterned PDMS stamps. (a) Schematics of the membrane transfer with PDMS1-stamp and PDMS2-stamp. (b-d) Microscope images of (b) alignment and pick-up of the diamond membrane using PDMS1-stamp, (c) the membrane flipping using PDMS2-stamp, (d) membrane placement onto the intermediate wafer coated with resist.

1.3 Intermediate wafer preparation

Intermediate wafers we used are $13\,\mathrm{mm}$ by $13\,\mathrm{mm}$ double side polished fused silica substrates. In principle, any polished transparent substrate can serve as intermediate wafers. Prior to dicing, the wafer was lithographically patterned and ICP-etched to form $5\,\mu\mathrm{m}$ tall pillars at the center of each chip. The size of the pillar is $400\,\mu\mathrm{m}$ by $400\,\mu\mathrm{m}$, shown as the largest square in Figure S1

(d). These elevated pillars are critical to compensate for the weakly defined approaching angle of the micropositioner on the transfer station. Pillars can also help protect existed structures on the final wafer.

Prior to the membrane transfer, intermediate wafers were spin-coated with a thin layer of positive photoresist (AZ 1505, Microchemicals GmbH, $\approx 500\,\mathrm{nm}$) or electron beam resist (950 K PMMA A4, MicroChem, $\approx 250\,\mathrm{nm}$). Positive resists are necessary in this process due to their much reduced viscosity after reaching the softening temperature, which grants smooth detachment in heated environments post plasma-activated bonding. When the membrane was flipped and placed on a pillar, it was released from the PDMS2-stamp due to stronger adhesion of the resist. The PDMS2-stamp-covered surface (the damaged side) was exposed again for the subsequent etching step.

1.4 Damaged layer removal via multi-cycle ICP etching

As will be discussed in section 2.1, out-of-plane strain resulted from He^+ implantation barricades effective bonding. The damaged layer also introduces considerable fluorescence background, which is not desirable for most optical measurements. We address these issues by removing the damaged layer via ICP reactive ion etching (RIE) (Plasma-Therm ICP Chlorine Etch). This step also defines the thickness of the membrane. We note that this intermediate wafer approach is generic and can be applied to HSQ-based membrane transfer as well to protect the final wafer from being etched.

We developed a multi-cycle Ar/Cl_2-O_2/Cl_2-O_2 etching sequence, limiting the effective etching time to $15\,\mathrm{s}$ per cycle. Cycles are separated by 3 pump-and-purge sequences to remove the gaseous residue, maintaining a consistent chamber environment and thus a constant etching rate. Compared to continuous etching, this multi-cycle procedure also prevents the resist from softening by keeping the sample temperature low.

1.5 Plasma treatment on diamond bonding interface

We use a downstream plasma asher (YES-CV200 RFS Plasma Strip/Descum System, Yield Engineering Systems Inc.) to activate bonding interfaces. Although other gas options (N_2, Ar, etc.) are possible[2], we choose O_2-based plasma for the surface functionalization due to their better performance on diamond and other materials[3,4]. In this work, we use two recipes on diamond membranes and carrier wafers, referred as the O_2 descum and the high power recipe. Both recipes are run at room temperature, since a degradation of hydrophilicity is observed after a brief baking ($90\,^\circ\mathrm{C}$ on a hot plate for $1\,\mathrm{min}$) post plasma treatments, as discussed in section 2.4.

We compare the two recipes according to three metrics measured on the resulting products, namely, surface morphology, surface hydrophilicity, and the optical performance of GeV^- and NV^- centers, and assessed the effects on both carrier wafer and diamond membrane surfaces. Results are discussed in section 2.2, 2.4, 3.2 and 3.4. For the carrier wafer choices, we tested fused silica and thermal oxide silicon. Both recipes lead to enhanced surface hydrophilicity while maintaining good surface morphology, which are favorable for the subsequent bonding

process. We expand the high power recipe to all carrier substrates used in this work due to the better hydrophilicity state it prepares. For diamond membranes, while both recipes could improve the signal to background ratio for optical characterizations of color centers, we did observe increased number of particle-like contaminates under atomic force microscopy (AFM) on the treated surfaces post high power recipes. We therefore employ the O_2 descum recipe for diamond membrane as a standard process except for NV^- sensing applications which requires a more adequate charge state preparation. The contamination can be eliminated by switching to more specialized tooling.

We note that the surface activation on the target substrate alone is effective for the bonding process, with the bonding quality as good as the ones with O_2 descum treatment. However, the lack of membrane treatment could result in a higher optical background, as discussed in section 3.2. Nonetheless, it provides an option for diamond membrane systems that are, for example, sensitive to O_2 plasma.

1.6 Direct bonding of the diamond membrane

The schematics of the bonding process is shown in Figure S2 (a). To start, the intermediate wafer is mounted on a glass cantilever controlled by a micropositioner (Signatone CAP - 946) using a flat, chip size PDMS stamp. The target substrate is held to a temperature-controlled stage by vacuum. Due to the lack of full tilt angle control of the micropositioner, we could only set the approaching angle to 0° along one direction, leaving the other to be a small but weakly defined value. A bright-field camera allows us to monitor the diamond membrane through the transparent PDMS and intermediate wafer and align it to the desired location on the target substrate. The alignment precision is $30\,\mu\mathrm{m}$, and the in-plane angle precision is 0.1°, both limited by the micropositioner tilt angle used in this work. Post alignment, we slowly bring down the intermediate wafer until part of the membrane is in contact with the target substrate, indicated by an appearance of interference pattern as exemplified in Figure S2 (b). We then step-wise increase the temperature ($75\,^\circ\mathrm{C}$, $95\,^\circ\mathrm{C}$, and $125\,^\circ\mathrm{C}$ for AZ 1505, $90\,^\circ\mathrm{C}$, $130\,^\circ\mathrm{C}$, and $170\,^\circ\mathrm{C}$ for PMMA) , allowing the resist to reach thermal equilibrium at each stage. Abrupt temperature changes can cause undesirable resist re-flow across regions and impact the bonding quality. Once the temperature reaches the highest stage, the resist layer thoroughly softens, and the intermediate wafer tends to shift translationally to release stress, as shown in Figure S2 (c). Next, the intermediate wafer is slowly moved away from the membrane and lifted via the motorized stage, leaving the membrane on the target substrate covered by some residual resist, as shown in Figure S2 (d). Finally, the bonded heterostructure is left to cool down till room temperature, preparing for the subsequent annealing. Stripping resist prior to the annealing is not recommended because of the weak bonding quality at this point.

1.7 Membrane annealing and resist removal

The quality of the plasma-activated bonding highly depends on the formation of the covalent bonds, which can be greatly strengthened by additional annealing. The annealing can also remove the $-$OH bonds inside the bonding interface if present[3,4]. We anneal the heterostructure

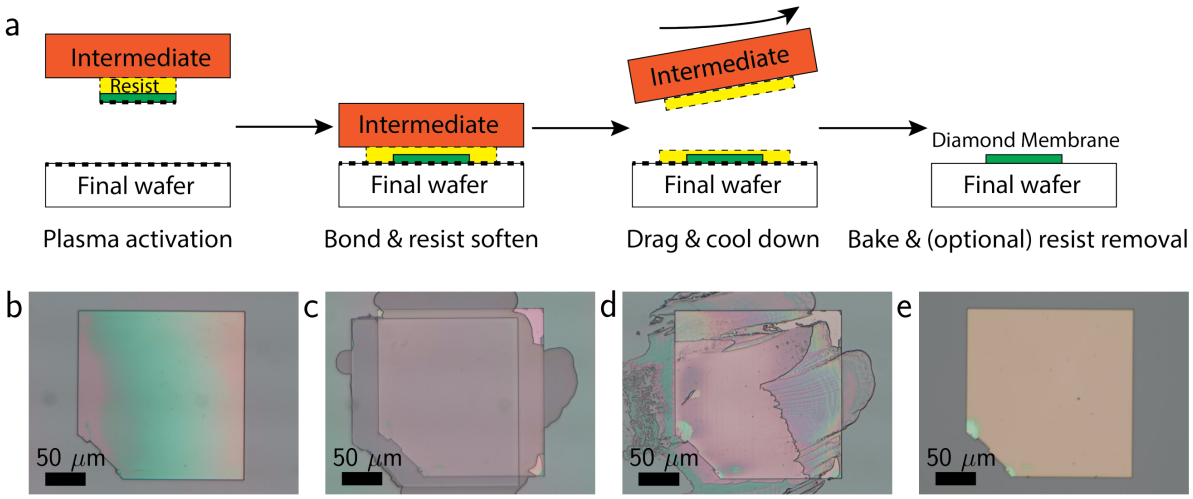

Figure S2: Plasma-activated membrane bonding. (a) Schematics of the bonding process. (b)-(e) Microscope images of (b) membrane alignment and initial contact, with the interference pattern induced by a non-zero approaching angle, (c) membrane bonded to the target wafer with resist re-flow at elevated temperatures, (d) the bonded membrane with residual resist after lifting the intermediate wafer, (e) the membrane post baking and optional resist removal. Here the AZ 1505 photoresist was applied which requires a di-acid clean, but PMMA-based bonded membrane is clean post annealing.

at $550\,^{\circ}\mathrm{C}$ for $8\,\mathrm{h}$ to $14\,\mathrm{h}$ in argon forming gas environment ($96\,\%$ of Ar, $4\,\%$ of H_2, $\approx 1\,\mathrm{atm}$), which eliminates potential oxidization on the diamond surface. Bonding strength when annealed at $450\,^{\circ}\mathrm{C}$ is not sufficient as the membrane can detach from the carrier substrate during acid cleaning. This might be explained by a less inert diamond surface to oxygen when the temperature exceeds $450\,^{\circ}\mathrm{C}$, which is about the temperature for standard diamond oxygen termination[5].

If PMMA is applied to the intermediate wafer, the residual resist will be fully baked out post annealing.[6] We thus only apply a brief O_2 descum to clean the surface. However, if AZ 1505 is used instead, the photoresist will crosslink post baking, which requires boiling di-acid cleaning (1:1 H_2SO_4:HNO_3 for $2\,\mathrm{h}$ at the nitric boiling point). Due to the much reduced viscosity of AZ 1505 compared with PMMA, we applied PMMA-based bonding on structured surfaces and acid-sensitive substrates, while using AZ 1505 on other substrates. The final device is shown in Figure S2 (e). We note that our bonded heterostructure is compatible with isopropyl alcohol, acetone, potassium or tetramethylammonium hydroxide (TMAH) based developers (such as AZ 300 MIF or AZ 400K), heated ($80\,^{\circ}\mathrm{C}$) N-Methyl-2-pyrrolidone (NMP), and room temperature NanoStrip. However, the tri-acid cleaning (1:1:1 H_2SO_4:HNO_3:$HClO_4$ at refluxing temperature), hot ($\geq 80\,^{\circ}\mathrm{C}$) Piranha (3:1 H_2SO_4:H_2O_2), and hot NanoStrip may damage the bonds and loosen the membranes from the target wafer.

2 Material characterizations

2.1 Out-of-plane strain of smart-cut membranes

Unlike isotropically-etched diamond frames[7] or ICP-etched diamond slabs[8], smart-cut diamond membranes naturally contain out-of-plane strain originated from the lattice mismatch between the damaged layer generated from He^+ implantation and the subsequent overgrowth layer. This strain brings a curvature to freestanding membranes due to their high geometry aspect ratio (usually beyond 500), and has been observed in previous works[9]. To roughly estimate the strain magnitude, we performed Raman spectroscopy on a transferred diamond membrane with $100\,\mathrm{nm}$ overgrowth layer prior to ICP etching. The experimental data is shown in Figure S3 (a) as individual points, which can be fit by two Lorentzian curves. The original membrane (He^+ damaged layer) is indicated as the dashed blue curve with a center wave number of $1326\,\mathrm{cm}^{-1}$, while the overgrowth layer obtains a center wave number of $1332\,\mathrm{cm}^{-1}$, labelled as the dashed orange curve. Differences in wave number indicate a $\approx 0.5\,\%$ lattice mismatch.

In Figure S3 (b) a test membrane partially attached to a PDMS2-stamp is shown, with the upper and lower parts floated, as pointed by the red arrow. From the interference pattern we can observe the extension of the original layer and the compression the overgrowth layer, leading the membrane to be curved up. The strain elimination via ICP etching is discussed in section 1.5.

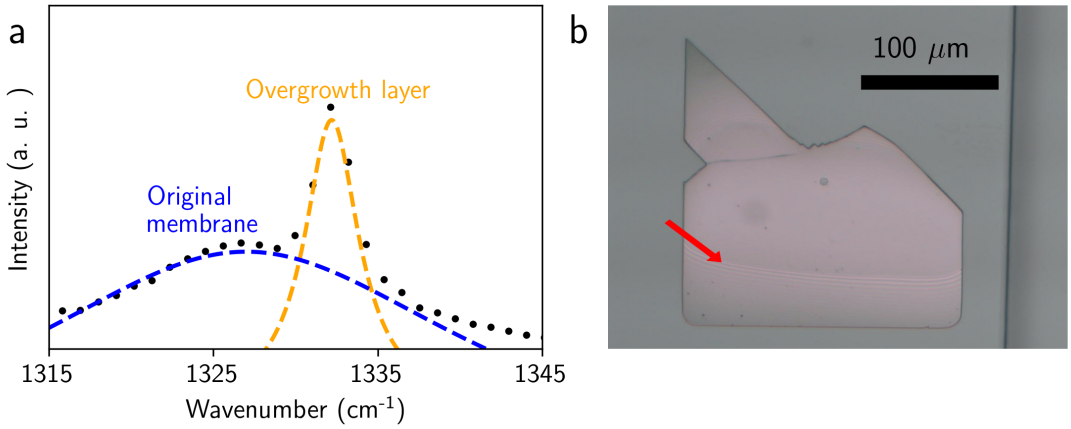

Figure S3: The out-of-plane strain in smart-cut diamond membranes. (a) Raman spectroscopy of a transferred membrane prior to the ICP etching. The raw data (black dots) can be qualitatively fitted by two separate peaks, the damaged (dashed blue line) and the overgrown (dashed orange line) layers. (b) A microscope image of a curved membrane on a PDMS2-stamp. The interference pattern pointed by the red arrow originates from the airgap between a curved membrane and a flat PDMS surface.

2.2 Surface morphology of diamond and final wafers

The success of plasma-enhanced bonding highly depends on the surface morphology of the diamond membrane and target substrates. We performed AFM to characterize the surface roughness along the fabrication process. Both small ($200\,\mathrm{nm}$ by $200\,\mathrm{nm}$) and large ($10\,\mu\mathrm{m}$ by $10\,\mu\mathrm{m}$) scale scans were applied to capture features of various sizes.

For diamond membrane surfaces, we only discuss the etched side in this section since the growth side preserves the excellent surface morphology as discussed in our previous work[1]. Prior to the ICP etching, the etched side has an R_q of $1.17\,\mathrm{nm}$ due to the He^+ implantation and EC etching. By applying 15 cycles of Ar/Cl_2 etching discussed in section 1.4, we show a polishing effect with R_q reduced to $0.54\,\mathrm{nm}$ ($0.44\,\mathrm{nm}$) in small (large) area scans, as shown in Figure S4 (a)-(b). We note that small area scans usually reveal greater roughness compared to large area scans, which might indicate the Cl-based contamination on the diamond surface as discussed in previous studies.[8] Such contamination can be removed by O_2/Cl_2-O_2 ICP cycles, shown as an R_q of $0.25\,\mathrm{nm}$ ($0.34\,\mathrm{nm}$) in small (large) areas (Figure S4 (c)-(d)). We did not observe the change of R_q post O_2 descum treatment ($0.28\,\mathrm{nm}$ and $0.34\,\mathrm{nm}$ in small and large area scans), as depicted in Figure S4 (e)-(f). In contrast, our customized plasma recipe is found to have a negative impact on the surface morphology by elevating the R_q to $0.84\,\mathrm{nm}$ ($1.09\,\mathrm{nm}$) in small (large) areas. This can be interpreted as an appearance of particle-like dust since the R_q of the contamination-free area remains to be $\leq 0.35\,\mathrm{nm}$. Such contamination can be reduced by transitioning to process specific tooling.

We also analyzed the impact of downstream plasma asher recipes on two widely used carrier substrates, namely fused silica and thermal oxide silicon wafer. Values of R_q are shown in Table S1. Both wafers exhibit sub-nm R_q out of the box, and their surface morphology is maintained post ashing with no correlation to power or duration settings. Therefore, we conclude that our plasma recipe has no significant effect on the surface morphology of these carrier wafers.

Carrier wafer type	AFM area	No plasma	O_2 descum	Custom O_2 plasma
Fused silica	$200\,\mathrm{nm}$ x $200\,\mathrm{nm}$	$0.324\,\mathrm{nm}$	$0.281\,\mathrm{nm}$	$0.366\,\mathrm{nm}$
	$10\,\mu\mathrm{m}$ x $10\,\mu\mathrm{m}$	$0.685\,\mathrm{nm}$	$0.581\,\mathrm{nm}$	$0.528\,\mathrm{nm}$
Thermal oxide	$200\,\mathrm{nm}$ x $200\,\mathrm{nm}$	$0.257\,\mathrm{nm}$	$0.290\,\mathrm{nm}$	$0.352\,\mathrm{nm}$
	$10\,\mu\mathrm{m}$ x $10\,\mu\mathrm{m}$	$0.270\,\mathrm{nm}$	$0.427\,\mathrm{nm}$	$0.293\,\mathrm{nm}$

Table S1: R_q of fused silica and thermal oxide wafers under various plasma recipes.

2.3 Height variation across diamond membranes

2.3.1 One dimensional (1D) height detection via profilometry

In this work two methods are applied for global flatness characterizations. For 1D characterization presented in the main text, we use a profilometer (Dektak XT) to scan across the membrane. The scan range is $350\,\mu\mathrm{m}$ with a $6.5\,\mu\mathrm{m}$ height detection limit. The membrane shows a height variation σ of $\approx 1\,\mathrm{nm}$, which is 10 times smaller than our HSQ-bonded membranes' value mea-

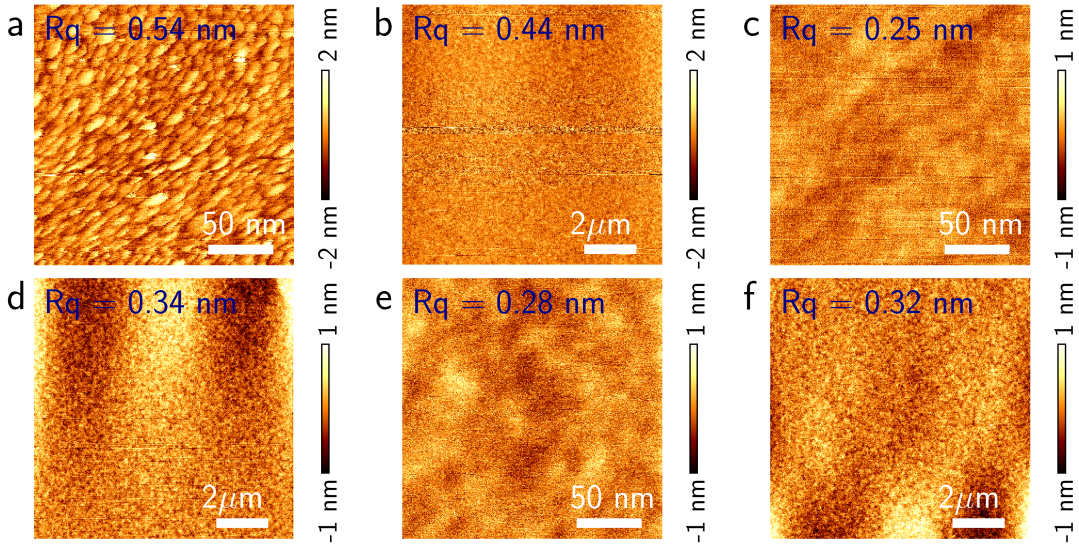

Figure S4: Small (200 nm scanning range) and large (10 µm scanning range) area AFM of the etched side of diamond membranes under various plasma conditions. (a)-(b) Post 15 Ar/Cl_2 cycles with recipe described in section 1.4. (c)-(d) Post additional 3 O_2/Cl_2-O_2 cycles with recipe described in section 1.4. (e)-(f) Post O_2 descum recipe described in section 1.5. The global patterns in (d) and (f) reflects the flattening fitting of the resist layer with height variation which is not related to the membrane surface morphology.

sured on the same equipment[1]. This σ is also below the minimum detectable height of the tool (10 nm) and the instrument resolution (1.5 nm) for large scale scanning.

2.3.2 Two dimensional (2D) height mapping via confocal laser scanning microscopy (CLSM)

The 2D membrane height map and surface topology is measured via an Olympus LEXT OLS4100 405 nm laser confocal microscope. The microscope image of the measured membrane-thermal oxide silicon heterostructure is shown in Figure S5 (a) with its height map shown in Figure S5 (b). The bonded membrane profile reveals a uniform height of 309 ± 8 nm across the membrane, with the standard deviation σ below the height resolution of the CLSM ($\approx$10 nm). Currently, the dominant sources of height inhomogeneity are assigned to diamond membrane crystallographic growth defects[10] and transfer process contamination, which can be minimized by performing the totality of the processing in a clean environment (e.g. cleanroom).

2.4 Hydrophilicity characterization of bonding interfaces

2.4.1 Contact angle measurement setup

We measure water contact angle to characterize the surface hydrophilicity of diamond and target substrates. Measurements were performed using a Kruss DSA100A dropped shape analyzer. DI water was dispensed from a sterile syringe (14-817-25, Fisher Scientific) through a thin needle

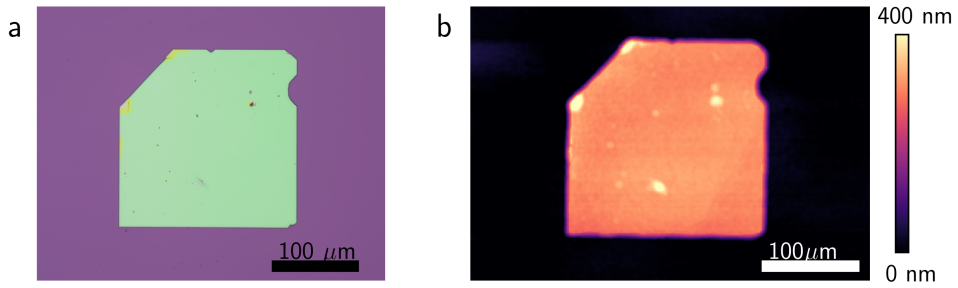

Figure S5: CLSM of a membrane bonded to a thermal oxide silicon substrate. (a) The microscope image of the characterized heterostructure. Several growth defects are present on this specific diamond membrane. (b) The 2D height map of the diamond membrane, showing an average height of 309 ± 8 nm. This data had a plane-fit adjustment performed to remove any substrate tilt aberrations. The X-Y resolution is quoted as $\leq 0.2\,\mu$m, whereas the Z resolution is hardware defined to ≤ 10 nm.

(75165A761, McMaster-Carr). The dispense rate was set to $2.67\,\mu\mathrm{L\,s^{-1}}$, resulting in a typical droplet size between $4\,\mu$L to $5\,\mu$L. The diamond we used for contact angle measurements are 3 mm by 3 mm single crystal fine-polished diamond substrates ($R_q \leq 0.3$ nm). Figure S6 (a)-(b) show the contact angle analysis of diamond and thermal oxide substrates before and after high power plasma ashing, indicating an improvement of the surface hydrophilicity. We note that the weaker O_2 descum recipe showed minimal influence on diamond hydrophilicity, with the contact angle above $40°$ (not shown in the figure).

2.4.2 Aging and temperature dependence of the surface hydrophilicity

As stated in previous studies,[11] surface hydrophilicity is positively correlated to the plasma-activated bonding quality. Here we characterize the decay of the hydrophilicity by recurring measurements of contact angle on various substrates, including diamond, fused silica, thermal oxide, sapphire and lithium niobate on insulator. The aging trend of the hydrophilicity is shown in Figure S6 (c), indicating the need for a timely bonding process. We also tested the temperature dependence of the hydrophilicity by baking the plasma-treated diamond sample on a $90\,°$C hotplate for 30 s prior to the contact angle measurements. A decay of hydrophilicity was observed, as shown in Figure S6 (d), possibly due to the loss of surface-absorbed water molecules. Partially due to the strong association between elevated temperature and reduced hydrophilicity, we chose resist AZ1505 as one of the mounting media in our bonding process for its much reduced viscosity at a fairly low glass transition temperature (softening temperature), see section 1.3.

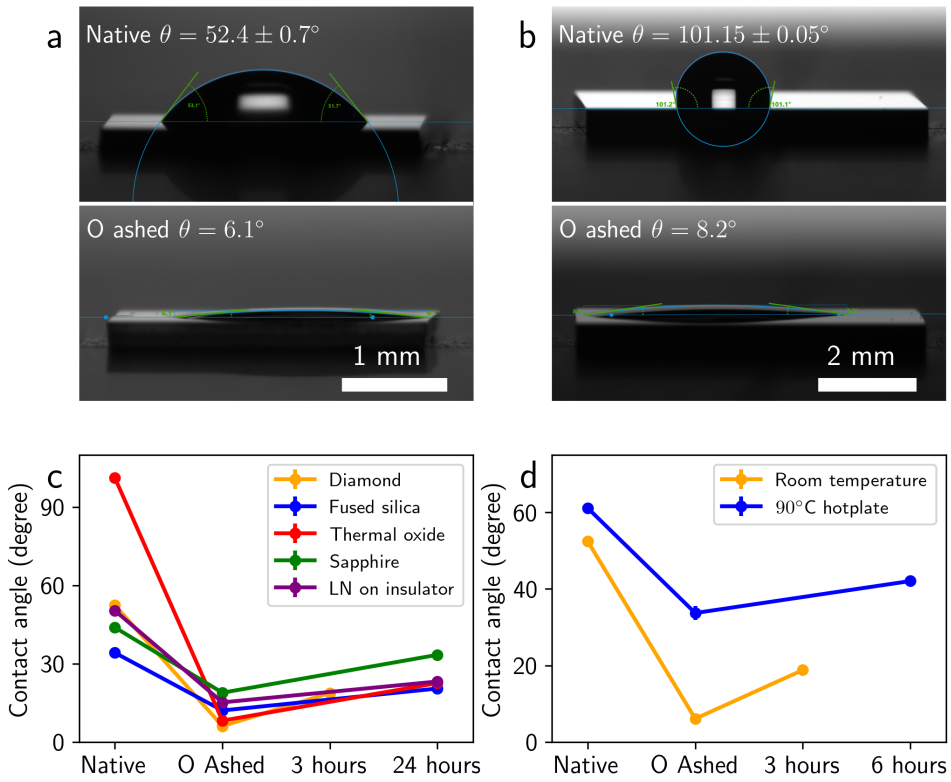

Figure S6: Surface hydrophilicity characterization via contact angle measurements. (a)-(b) Contact angles of native (top) and high power plasma-treated (bottom) diamond and thermal oxide substrates. (c) Aging of hydrophilicity on various substrates. (d) Hydrophilicity of diamond surface with (blue) or without (orange) 30 s baking on a 90 °C hotplate.

2.5 High resolution transmission electron microscopy (HRTEM) and Energy-dispersive X-ray spectroscopy (EDS)

To obtain an atomic level understanding of the bonding interface, we performed HRTEM on a cross-sectional sample from a diamond-sapphire heterostructure. The sapphire substrate is C-axis (0001) from University Wafer. To start, a 200 nm-thick gold mask was deposited on the surface to protect the diamond membrane being damaged by Ga ion beam. Using a Zeiss NVision 40 system, a cross-sectional TEM specimen with thickness of a few tens of nanometer was prepared by standard FIB lift-out procedure. The HRTEM image was obtained by a FEI Titan operated at 200 kV, which was equipped with aberration corrector and chromatic corrector. The scanning transmission electron microscope (STEM) image was acquired by using high-angle annular dark field (HAADF) detector, as shown in Figure S7 (a). A FEI Talos S/TEM equipped with a Super X energy-dispersive spectrometer (EDS) was employed for STEM-EDS elemental mapping. The result is shown in S7 (b)-(d).

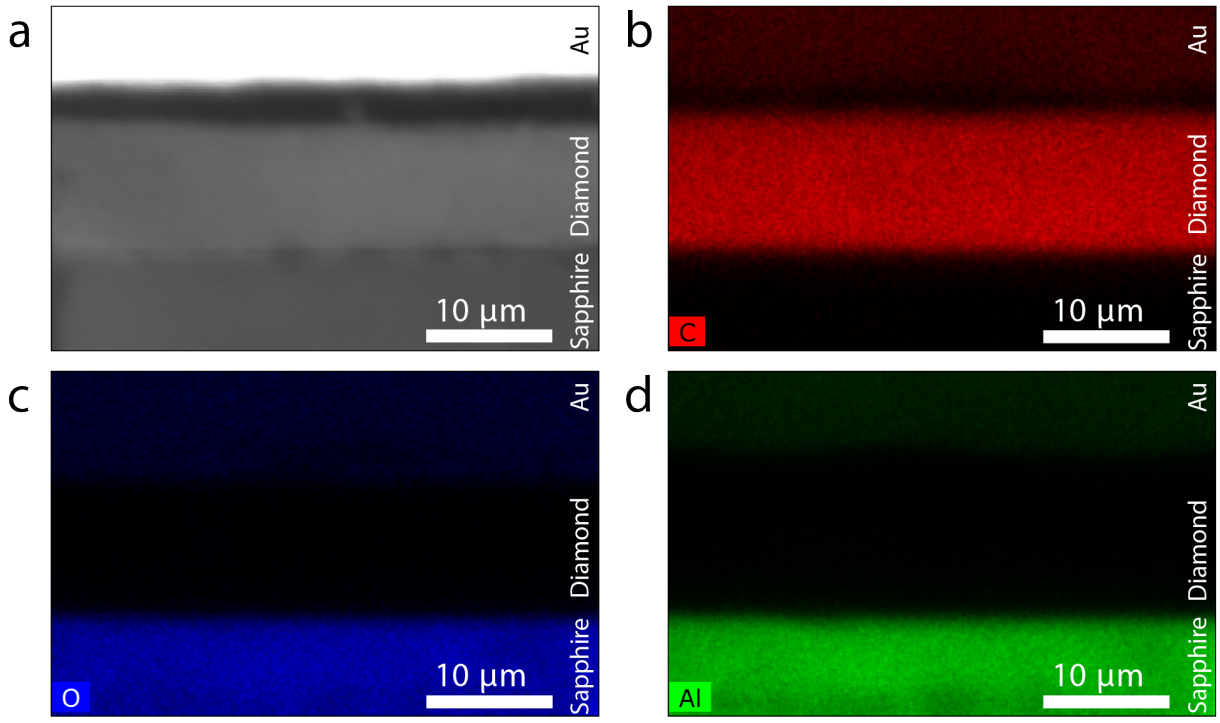

Figure S7: Additional atomic scale analysis of the bonded membrane. (a) HAADF-STEM of the diamond-sapphire heterostructure. (b)-(d) STEM-EDS elemental analysis of the diamond-sapphire heterostructure. The intensity of carbon, oxygen and aluminum elements at the cross section is shown in (a), (b) and (c), respectively.

2.6 X-ray photoelectron spectroscopy (XPS)

The experimental samples were identical to those employed in the rest of the demonstrations: diamond, fused silica, and sapphire. A set of these was left unprocessed to be used as a reference, whereas the other set received surface activation via oxygen plasma ashing $\approx 90\,\mathrm{min}$ before loading into the XPS chamber. Two different incidence angles were taken for the XPS analysis to confirm that the perceived effect was related to near-surface species. One set of characterization was taken at 0° incidence, with another set taken at 35° incidence. No significant differences were found for both datasets, as such only the 0° incidence dataset is shown. In agreement with the contact angle measurements, in that timeframe, the surface is known to have degraded somewhat, however it remains 'bond-ready'. As such, all the quantitative XPS analysis provides a lower bound on the surface activation related species. Future experiments will be necessary to study the 'as-ashed' surfaces.

An Al-Kα source in a Thermo Scientific ESCALAB 250Xi was used to perform the XPS characterization at both normal and 35° incidence angles. Elemental peaks were taken with a pass energy of $50\,\mathrm{eV}$, $50\,\mathrm{ms}$ dwell time, and a step size of $0.1\,\mathrm{eV}$, whereas the C KLL peak had $100\,\mathrm{eV}$ pass energy and $0.5\,\mathrm{eV}$ step size. For all scans, a charge compensating electron flood gun was used whereas the X-ray spot size was maintained at $\approx 200\,\mu\mathrm{m}$ in spread. C 1s, C KLL, Al 2p, Si 2p, O 1s, N 1s peaks were all collected in high-resolution mode and the presence of other

unplanned contaminants was verified via survey scans. All scans were references to the C sp^3 peak at $284.8\,\mathrm{eV}$ binding energy (BE). Elemental analysis was taken by quantitative comparison of the high-resolution components fits (with appropriate sensitivity factors accounted for). The C 1s KLL signature was used to extrapolate and corroborate sp^2-to-sp^3 ratio obtained from the C 1s line-fit by calculating and fitting the peak-to-peak separation of the first derivative of the KLL signal[12,13]. All peak fitting parameters were taken from commonly agreed on values for equivalent materials and systems from the NIST XPS database.[14] XPS high-resolution spectra of relevant lines with fitting parameters are shown in Figure S8 and Figures S17, S18, S19, S20, and S21 in the section 6 for the Unprocessed-Diamond, Ashed-Diamond, Unprocessed-Sapphire, Ashed-Sapphire, Unprocessed-Silica, and Ashed-Silica, respectively. The analysis is quite consistent with the conclusions of this paper. However, an unresolved abnormality needs to be pointed out, specifically the presence of an unidentified third component of the O 1s peak in the fused silica samples. While currently that peak is identified as organics, this is a placeholder title. Looking at the appearance of an intermediate SiO_2-Silicate peak in the fused silica Si 2p quantification, it is plausible that these are the oxygen species from low coordination quartz. However, at this time further experiments would need to confirm this hypothesis. Regardless, these are in the low $\mathrm{at.\%}$ range ($\approx 2\,\mathrm{at.\%}$) and do not impact any of the conclusions of this paper. Table S2 presents the full quantification summary of the XPS experiments.

XPS Quantification (at.%)

Peak - Component	Diamond Raw	Diamond Ashed	Sapphire Raw	Sapphire Ashed	Silica Raw	Silica Ashed
C 1s - sp3	75.6	77.9				
C 1s - sp2	6.5	5.9	5.9	5.4	3.7	2.0
C 1s - C-O-C	8.6	8.2	0.3	0.5	1.7	0.8
C 1s - C=O	1.6	1.3	1.0	0.8	0.8	0.5
C KLL - sp2	12.8 ± 3	4.5 ± 3				
O 1s - C=O	3.3	2.0	4.5	8.4		
O 1s - C-O	4.2	4.5				
O 1s - Al/Si Oxide			40.0	38.3	51.9	53.8
O 1s - Substochio.			3.4	3.9	0.9	0.7
O 1s - Un-ID.					2.1	2.6
Al 2p - Oxide			42.0	39.7		
Al 2p - Substochio.			2.8	3.0		
Si 2p - SiO2					16.6	18.7
Si 2p - Un-ID.						1.6
Si 2p - Silicate					22.1	18.9
N 1s - Adsorbed N	0.2	0.1	0.2	0.1	0.3	0.2

Table S2: High-resolution XPS quantification for all the fitted components and peaks.

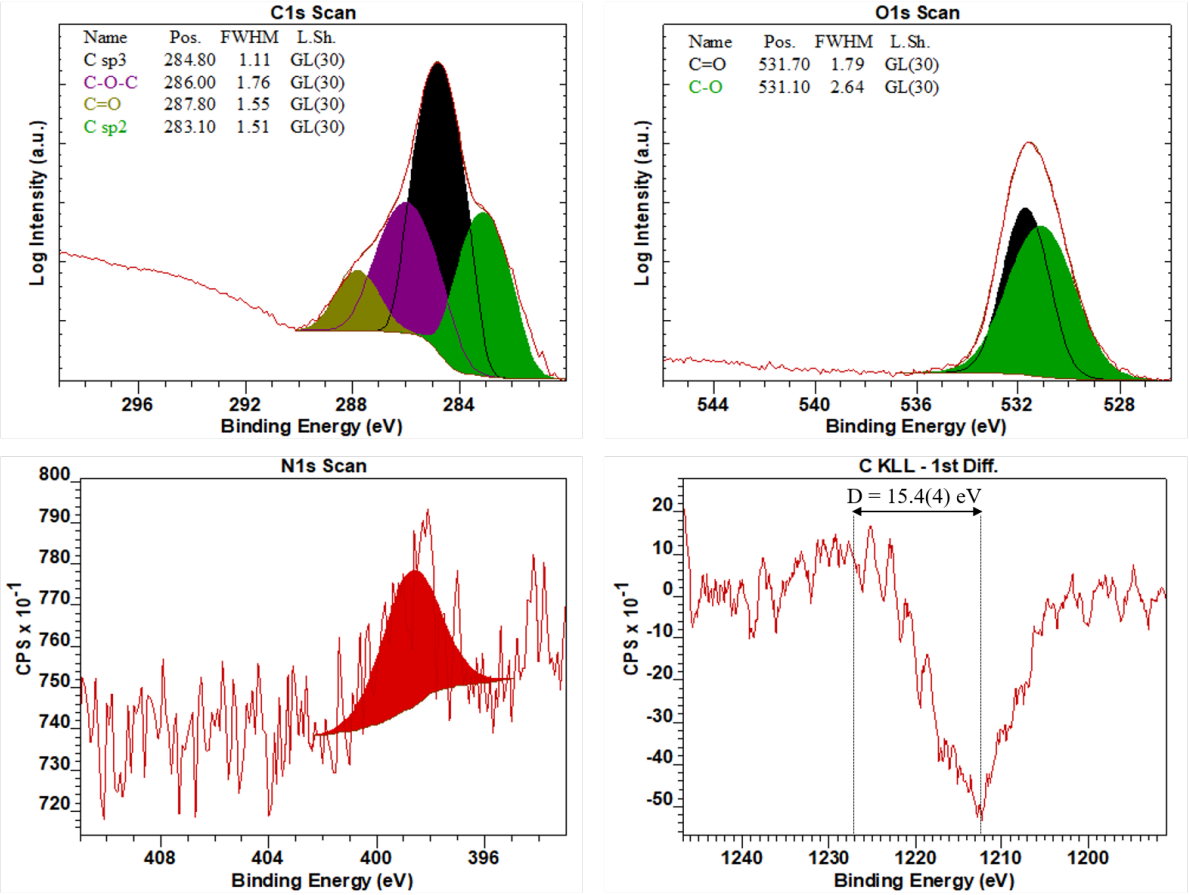

Figure S8: XPS characterization of the unprocessed diamond substrate, showing the C 1s and O 1s deconvolutions with component labels and fitting parameters. sp^2 content quantification is achieved via D parameter linear extrapolation of the C KLL first order derivative[12,13]. N 1s peak contamination also showed as samples were exposed to atmosphere. Some of the peak fittings are presented in log scale to help discern minority components.

3 Optical characterizations of GeV^- and NV centers

3.1 Optical setup

In this work, membrane samples are mounted inside a closed-loop cryostation (Montana S200) and cooled down till $4\,\mathrm{K}$ for low temperature measurements. The position of the membrane is controlled by three closed-loop piezo micropositioners (Attocube ANC 350). Light beams are navigated by a fast steering mirror (Newport FSM-300). For photoluminescence (PL) measurements, we either use a $519\,\mathrm{nm}$ green diode (Thorlabs LP520-SF15) or a $532\,\mathrm{nm}$ continuous wave (CW) laser (Lighthouse Photonics Sprout-G) as the excitation source. For photoluminescence excitation (PLE) measurements of GeV^-, the excitation laser is generated by a wave mixing module (AdvR Inc.) combining a tunable CW Ti:Sapphire laser (M Squared Solstis) and a monochromatic CW laser (Thorlabs, SFL 1550P). A single photon counting module (SPCM)

(Excelitas Technologies) is applied to plot PL maps, while a spectrometer (Princeton Instruments, SpectraPro HRS) is used to measure the spectra of the color centers. We combine two bandpass filters (Semrock FF01-615/24-25, Semrock FF01-600/14-25) for GeV^- PL measurements, and use bandpass filters ($2\times$ Semrock FF01-647/57-25) for PLE measurements. For NV measurements, a single long pass filter (Semrock LP02-561RE-25) is used to capture both NV^0 and NV^- signals.

3.2 Effect of plasma treatments on the optical coherence of GeV^- centers

As mentioned in section 1.5 and 2.2, oxygen plasma on diamond membranes is optional for the bonding process. In this section, we investigate the effect of the plasma on the PL and PLE properties of GeV^- centers. Two membranes, each has $\approx 200\,\mathrm{nm}$ thickness and contains $40\,\mathrm{nm}$-deep implanted GeV^- centers from the top surface, were transferred on a single thermal oxide wafer. The membrane 1 received no plasma treatment prior to the bonding, while the membrane 2 received a strong plasma ashing introduced in the section 1.5. Figure S9 (a)-(b) shows the $4\,\mathrm{K}$ PL map of the GeV^- centers on membrane 1 and 2, which clearly indicates a signal-to-background improvement via plasma treatments. The average background dropped from ≈ 7000 to ≈ 1900, leading to an improvement of signal-to-background ratio from ≈ 4.5 to ≈ 11. The slightly lower signal shown in Figure S9 (b) indicates a slight oxygen termination which shifts the Fermi level away from the optimal value for GeV^- centers. Figure S9 (c) shows the single scan ZPL linewidths with resonant excitation. We observed no statistical difference of the linewidth distribution, with mean single scan linewidth of $97\,\mathrm{MHz}$ ($85\,\mathrm{MHz}$) for membrane 1 (2). A separate characterization of tin vacancy centers in our membranes using higher resolution equipment reported a much narrower linewidth profile, with the average linewidth only $\approx 50\%$ higher than the transform-limited value[15], indicating a low charge noise environment.

3.3 Strain characterization via GeV^- centers

Group IV centers in diamond are good sensors for local strain environment due to their relatively large strain susceptibilities[16]. The strain magnitude can be estimated via the relative shift of the wavelength $|\epsilon_{A_{1g}} - \epsilon_{A_{1u}}|$ and the increased ground state splitting $2\sqrt{\epsilon_{E_{gx}}^2 + \epsilon_{E_{gy}}^2 + (\frac{\lambda_{SO}}{2})^2}$. We recorded spectra from 69 (52) GeV^- centers in diamond membranes direct-bonded to fused silica (thermal oxide) carrier wafers. The ZPL wavelength and ground state splitting distribution are shown in Figure S9 (d). Since implantation-induced strain has a large span which greatly affects GeV^-'s ZPL and ground state splitting statistics, we only focus on the color centers with ZPL from $601.5\,\mathrm{nm}$ to $603.2\,\mathrm{nm}$ and ground state splitting $\leq 800\,\mathrm{GHz}$ to estimate the strain from bonded membrane crystals. This region covers $\approx 80\,\%$ of our data points.

For membranes bonded to fused silica (thermal oxide) wafers, the average ZPL wavelength of GeV^- centers is $602.68(20)\,\mathrm{nm}$ ($602.53(8)\,\mathrm{nm}$), with the average ground state splitting to be $307(158)\,\mathrm{GHz}$ ($224(75)\,\mathrm{GHz}$). These ZPL wavelength distributions are comparable with those obtained in bulk diamonds.[17] We do observe a slight positive strain with diamond-fused silica heterostructures, which could be explained by the lower thermal expansion ratio of fused silica. Thermally induced negative strain is barely visible for diamond membrane-thermal oxide

substrates, which may come from the fact that membranes with such a high aspect ratio ($\geq$1000) could deform instead of generating negative strain under compressive stress. We estimate the average strain level of diamond membranes to be $\approx 2.9 \times 10^{-4}$ ($\approx -1.7 \times 10^{-4}$) on fused silica (thermal oxide) carrier wafers.

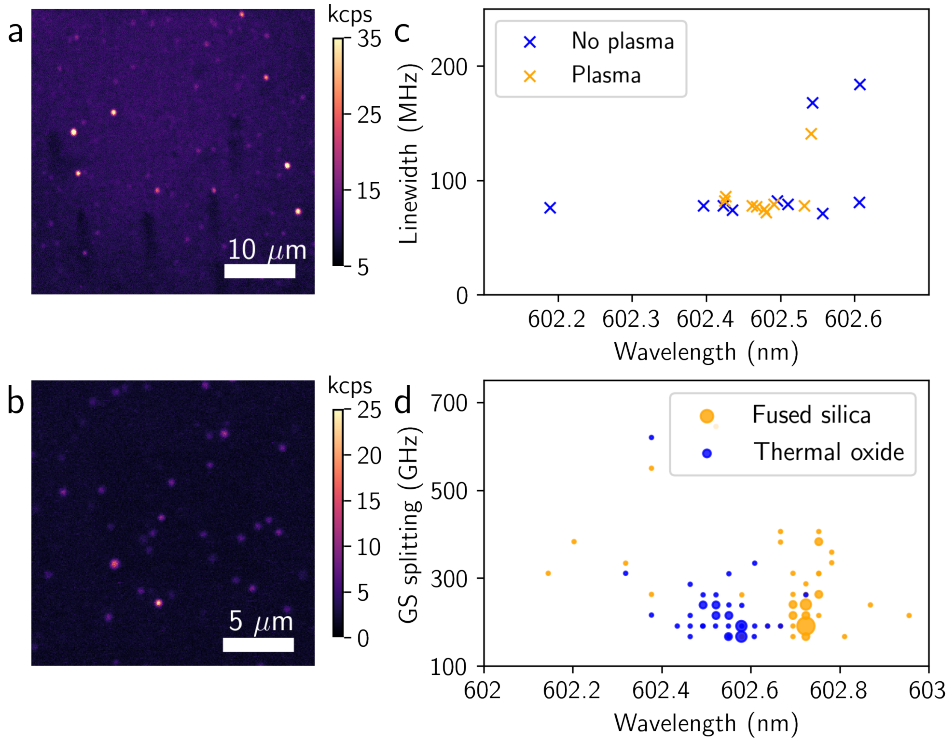

Figure S9: Additional optical characterization of GeV$^-$ centers in bonded membrane at 4 K. (a) A PL map of GeV$^-$ centers with no plasma treatments prior to the bonding. (b) A PL map of GeV$^-$ centers with diamond treated via high power plasma recipe. (c) ZPL wavelength and single scan linewidth distribution of GeV$^-$ centers. Centers from native (plasma treated) membranes are labelled in blue (orange). (d) ZPL wavelength and ground state splitting statistics of GeV$^-$ centers in diamond membranes bonded to fused silica (orange) or thermal oxide (blue) substrates. The size of each disk reflects the occurrence of the same data point within the resolution of the spectrometer ($\approx$0.04 nm or $\approx$30 GHz). This resolution also accounts for the artificial, equally spaced data pattern shown here.

3.4 NV centers at 4 K

Thanks to the low optical background of the direct bonding method, we were able to resolve individual NV centers in diamond membrane heterostructures. A typical NV PL map taken at 4 K is shown in Figure S10 (a), with a signal-to-background ratio of over 1.4. This paves the way of towards NV sensing applications, as discussed in the main text. In addition, the charge stability of NV centers is a good indicator of membrane's surface termination with respect to

various plasma treatments on the diamond bonding interface. Here we characterized the NV spectra in three bonded membranes. They were picked up from a single mother substrate doped *in-situ* with ^{15}N, thus contain same NV densities. They were bonded to SiO_2 surfaces with (1) no plasma treatment (2) O_2 descum (3) high power plasma ashing on the diamond bonding side. The typical NV spectra and statistical data is shown in Figure S10. We observe that with no plasma treatment, the NV center stays at the neutral charge state due to the hydrogen termination effect of the Ar/H_2 annealing process.[18] However, membranes treated with plasma have considerably higher NV^-/NV^0 ratio. This ratio is positively correlated with the strength of the O_2 ashing process, indicating a better oxygen termination performance which helps maintain the NV center in its negatively charged state[19]. Indeed, it is expected that such a dry O-termination method can be used to desirably engineer the diamond near-surface Fermi level for NV^- based applications[20,21]. Systematic characterizations of the effect of such plasma activation processing on near-surface NV^- are ongoing.

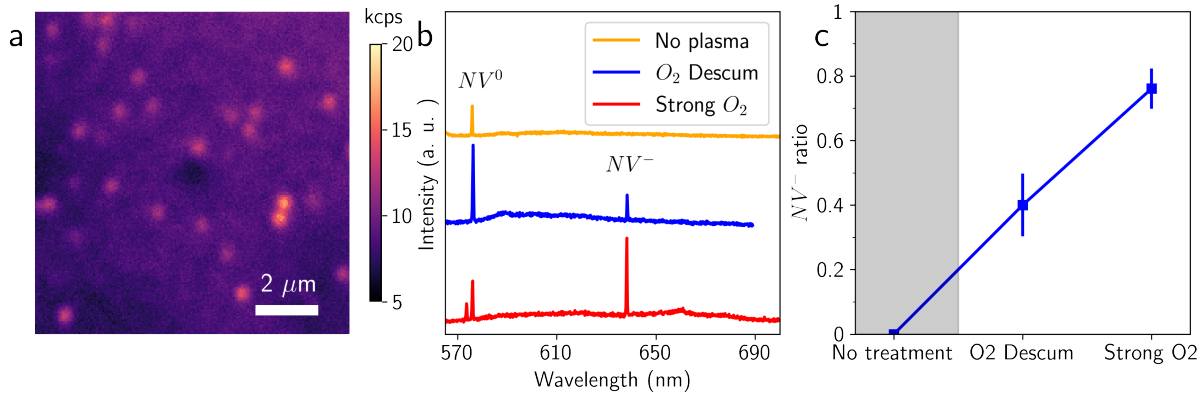

Figure S10: Additional optical characterization of NV centers in direct-bonded diamond membrane measured at $4\,\mathrm{K}$. (a) A PL map of NV centers in a diamond membrane with $325\,\mu\mathrm{W}$ green excitation and $561\,\mathrm{nm}$ longpass filter. The signal-to-background ratio is ≈ 1.4. (b) The spectra of NV centers with no plasma (orange), O_2 descum (blue) or high power O_2 plasma treatment (red) prior to bonding. The dominant NV^0 originates from the Ar/H_2 annealing. The appearance of NV^- indicates the surface oxygen termination of the diamond bonding interface. The small peak on the left side of the red curve is the Raman response of diamond due to the different excitation laser wavelength ($532\,\mathrm{nm}$ instead of $519\,\mathrm{nm}$). (c) The ratio of NV in its negatively charged state with respect to different plasma conditions on the diamond bonding interface. The NV^- ratio increased from 0 to $76(6)\,\%$. Calculation of this ratio takes the Huang-Rhys factor of NV^0 (3.3) and NV^- (4.0) into account.[22]

4 Nanophotonic cavities with direct-bonded diamond membranes

4.1 Optical setup for nanophotonic cavity measurements

A similar confocal setup as the $4\,\mathrm{K}$ one is used for cavity measurements, but the system operates at room temperature. Two separate beams controlled by galvanometer systems (Thorlabs GVS102) are applied to perform transmission spectroscopy. A pulsed supercontinuum source ($430\,\mathrm{nm}$ to $2400\,\mathrm{nm}$, SC-OEM YSL Photonics) is used for broadband excitation, and a spectrometer (Princeton Instruments, SpectraPro HRS) is used to observe the optical bandgap and measure the cavity resonance. Finer cavity linewidth measurements are performed by scanning a Ti:Sapphire laser (M Squared Solstis) around resonant wavelengths of the cavities. Transmission signal is collected by a SPCM (Excelitas Technologies).

4.2 TiO_2-based nanophotonic structures

4.2.1 Fabrication process of TiO_2 cavities

Our TiO_2 nanofabrication process is similar with the one described in previously.[23] The process starts with a $340\,\mathrm{nm}$ electron beam resist deposition (950 K PMMA A4, MicroChem), followed by a $20\,\mathrm{nm}$ gold deposition via thermal evaporation (Nexdep PVD platform, Angstrom Engineering) to prevent charging effects. Cavity patterns are lithographically defined at a dose of $1200\,\mu\mathrm{C\,cm^{-2}}$ at $100\,\mathrm{keV}$ (Raith EBPG5000 plus), and the gold layer is removed by TFA gold etchant (Transene) afterwards. Exposed patterns are developed in a 1:3 MIBK:IPA solution on a cold plate at $7\,^{\circ}\mathrm{C}$ for $90\,\mathrm{s}$, followed by a $60\,\mathrm{s}$ of IPA stopper and $60\,\mathrm{s}$ of DI water rinse. A $3\,\mathrm{s}$ ICP RIE etching is then conducted to remove the residual resist post developing. TiO_2 deposition takes place in an atomic layer deposition (ALD) system (Savannah Thermal ALD, Veeco) at $90\,^{\circ}\mathrm{C}$. The precursors of the TiO_2 deposition include tetrakis (dimethylamido) titanium (TDMAT) and water. The deposition thickness is $200\,\mathrm{nm}$ to $300\,\mathrm{nm}$, depending on the actual geometry of the structure. Overfilled TiO_2 is removed by another ICP RIE etch and the remaining resist is stripped by nanostrip (MicroChem). Finally, the structures are annealed at $250\,^{\circ}\mathrm{C}$ on a hotplate for $2\,\mathrm{h}$ to improve their optical quality. Scanning electron microscopy (SEM) images of fishbone cavities and ring resonators on the diamond membrane are shown in Figure S11 (a) and (b), featuring planarized top surfaces and smooth sidewalls.

4.2.2 Optical characterization of TiO_2 ring resonators

We measured the transmission of the TiO_2-diamond ring resonator through the drop port. The resonant excitation data for transverse electric (TE) and transverse magnetic (TM) modes are identified via separate polarization measurements. We observed high quality factors Q for both modes, with $Q_{TE} = 12620$ and $Q_{TM} = 16320$. The spectrum of the ring resonator and the resonant scan results are shown in Figure S11 (e). We note that this is the first demonstration of deposited TiO_2 ring resonators on diamond. Our current ring resonator design supports both

modes, but the quality factor for either mode can be further improved via geometry optimization.[24]

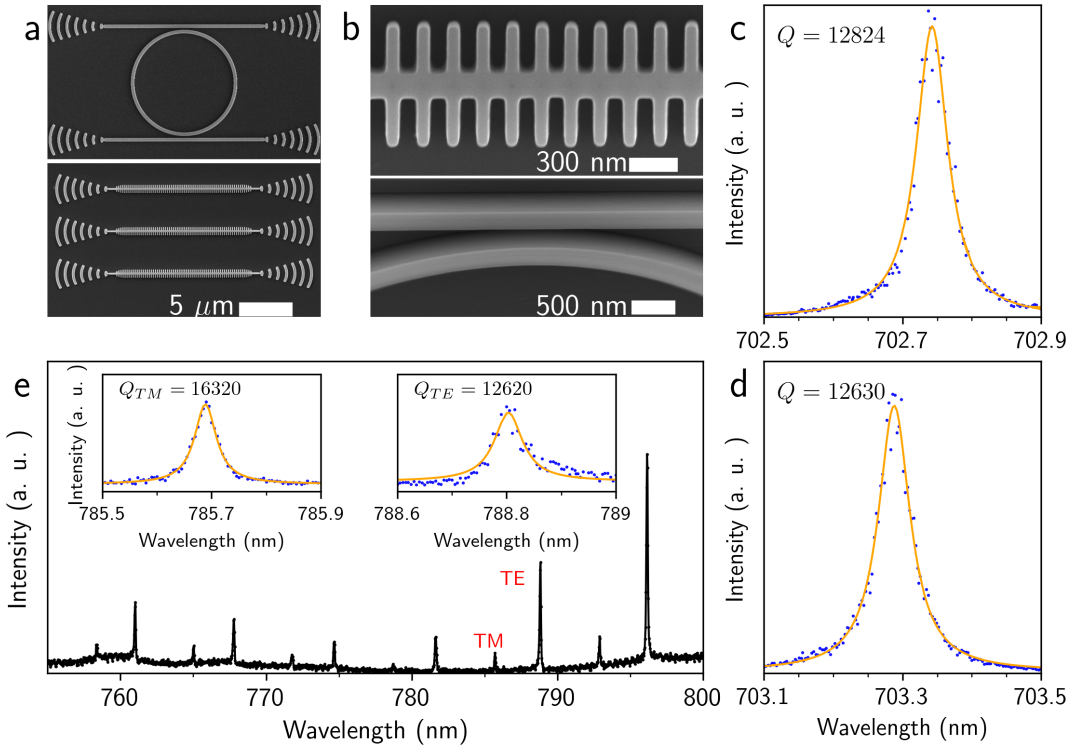

Figure S11: Additional information of TiO_2 nanophotonic devices. (a) Zoomed-out SEM images of fishbone cavities and ring resonators on diamond membrane. (b) Zoomed-in SEM images of fishbone cavities and ring resonators, featuring flat top surfaces and smooth sidewalls. (c-d) Quality factors Q_{TiO_2} of two best TiO_2 fishbone cavities directly fabricated on bare fused silica substrates. (e) The transmission spectrum of the TiO_2-based ring resonator measured at the drop port. Insets: the TE and TM cavity resonances measured with a tunable laser as the excitation source.

4.2.3 TiO_2 cavities on fused silica

To estimate the optical loss of the direct bonded diamond heterostructure, we repeated the TiO_2 fishbone cavity fabrication on bare fused silica substrates and measured their optical transmission via resonant excitation. The maximum quality factor Q_{TiO_2} we measured is $12\,824$, with the average Q_{TiO_2} of the two best cavities is $12\,727$, as shown in Figure S11 (c) and (d). This Q_{TiO_2} includes the optical scattering within the deposited TiO_2 and the surfaces of the cavity (top surface, interface between TiO_2 and fused silica, sidewalls etc.). Subtracting the average Q of TiO_2 cavities on diamond membrane returns an approximate optical loss of the bonded diamond-fused silica system, which is $Q_{sys} \approx 50000$. This system optical loss includes the

optical scattering from the diamond/fused silica interface, the diamond/TiO_2 interface and the diamond crystal itself, instead of the loss from the TiO_2/fused silica interface.

4.3 Fabrication process of diamond cavities with bonded membranes

Diamond membranes are thinned down to $280\,\mathrm{nm}$ and then bonded to a thermal oxide substrate with $1\,\mu\mathrm{m}$ oxide thickness for diamond-based nanophotonic structures. We first deposit a hard mask of $25\,\mathrm{nm}$ alumina via ALD (Savannah Thermal ALD, Veeco), then spin a $90\,\mathrm{nm}$ of electron beam resist (ARP6200.04, MicroChem), and thermally evaporates $20\,\mathrm{nm}$ of gold (Nexdep PVD platform, Angstrom Engineering) to prevent charging effects. Cavity patterns are lithographically defined at a dose of $250\,\mu\mathrm{C\,cm^{-2}}$ at $100\,\mathrm{keV}$ (Raith EBPG5000 plus), and the gold layer is removed by TFA gold etchant (Transene) afterwards. Exposed patterns are developed in a Amyl Acetate for $60\,\mathrm{s}$, followed by a $60\,\mathrm{s}$ of IPA stopper and $60\,\mathrm{s}$ of DI water rinse. A $30\,\mathrm{s}$ alumina ICP RIE etching is then conducted to transfer the pattern into the hard mask. This is followed by resist removal in heated NMP at $80\,^{\circ}\mathrm{C}$. We then conduct multiple cycles of ICP RIE etching with O_2/Cl_2-O_2 plasma in $15\,\mathrm{s}$ intervals till the diamond is etched all the way through. Lastly, we performed a $20\,\mathrm{s}$ of Al_2O_3 etching to remove the hard mask.

5 Heterostructure-enabled flow channel for molecular sensing applications

5.1 Widefield microscope setup

A custom-built widefield fluorescence microscope in an inverted configuration operated at room temperature was used to acquire all the widefield images presented in this section. It is equipped with a 60× oil objective (Olympus UPLAPO60XOHR) with $NA = 1.5$. A motorized translational stage allows the displacement of the focus point of the laser beam on the back focal plane of the objective, enabling a continuous change in excitation beam angle for episcopic and total internal reflection fluorescence (TIRF) illumination. Two independent laser sources ($488\,\mathrm{nm}$ and $532\,\mathrm{nm}$, $100\,\mathrm{mW}$ maximum power output, Coherent Sapphire) are available for excitation, and an Andor iXon Ultra 888 electron-multiplying charge-coupled device (EMCCD) is used for image collection. Unless otherwise stated, EMCCD was cooled down to $-60\,^{\circ}\mathrm{C}$ to minimize noise. We implement an iris in the excitation path to manually adjust the size of the laser beam. A Hamamatsu W-VIEW GEMINI system is placed in front of the EMCCD, which is usually operated in the bypass mode unless taking dual-imaging data.

5.2 Imaging of NV^--hosting diamond membranes

5.2.1 Widefield imaging

We bonded diamond membranes containing δ-doped NV^- to the center of $25\,\mathrm{mm}$ by $8\,\mathrm{mm}$ rectangular-shaped fused silica slabs diced from 2 inch wafers (Part#: U01-131121-1 from Uni-

versity wafer, $180\,\mu\mathrm{m}$ thick). One of these samples was characterized thoroughly as discussed thereafter. For simplicity, we refer this particular sample as Sample A. Diamond membranes from the same mother substrate as Sample A have been characterized previously[1]. We applied immersion oil (Olympus Type F) to the backside of the coverslip (opposite to the bonded diamond membrane) and imaged through it. A long-pass optical filter (Semrock LP594) was used. The maximum excitation power of the $532\,\mathrm{nm}$ laser when the beam size matches the effective field-of-view ($73\,\mu\mathrm{m}$ by $73\,\mu\mathrm{m}$) was $\approx 35\,\mathrm{mW}$, namely a power density of approximately $800\,\mathrm{W\,cm^{-2}}$. We note that a typical confocal setup for NV^- experiments operates with a power density of approximately $10\,\mathrm{kW\,cm^{-2}}$ to $100\,\mathrm{kW\,cm^{-2}}$, which is 1 to 2 orders of magnitude higher than our widefield imaging system. The micrograph shown in S12 (a) is a rotated version of Figure 4 (a) in the main text, which was acquired with $100\,\mathrm{s}$ exposure time and 300 gain. We use an iris to restrict the size of excitation beam to $\approx 35\,\mu\mathrm{m}$ in diameter, which avoids the direct illumination of the membrane edges. The fluorescence background of the diamond membrane region was very low, which is comparable and even appeared to be darker than the fused silica coverslip due to the large refractive index of diamond. The bright, diffraction-limit spots in the diamond membrane, later verified as predominately NV^- centers, showed excellent photostability under continuous excitation (would not be photobleached).

5.2.2 Confocal imaging and NV^- verification

We performed a confocal scan on Sample A shown in Figure S12 (a) and confirmed that the observed bright emitters in widefield image were mostly NV^- centers. This verification was done by measuring the optically detected magnetic resonance (ODMR) feature of NV^- centers with external microwave signals. The confocal scan and the continuous wave ODMR (CW-ODMR) were performed on a custom-built confocal microscope equipped with a fast steering mirror and a $520\,\mathrm{nm}$ laser as excitation ($70\,\mu\mathrm{W}$). Microwave signal was generated from a vector signal generator (Stanford research systems, SG394) and delivered to the sample through a $25\,\mu\mathrm{m}$-thick gold wire. Pulse control was achieved using a pulse streamer (Swabian Instruments Pulse Streamer 8/2). All measurements were done at room temperature with no external magnetic field. We characterized 14 bright emitters in a $10\,\mu\mathrm{m}$ by $5\,\mu\mathrm{m}$ area as shown in Figure S12 (f). The ODMR scanning range was between $2.82\,\mathrm{GHz}$ to $2.92\,\mathrm{GHz}$. As the result, 12 out of 14 emitters showed the characteristic NV^- ODMR feature centered at $2.87\,\mathrm{GHz}$ with $2\,\%$ to $6\,\%$ signal contrast.

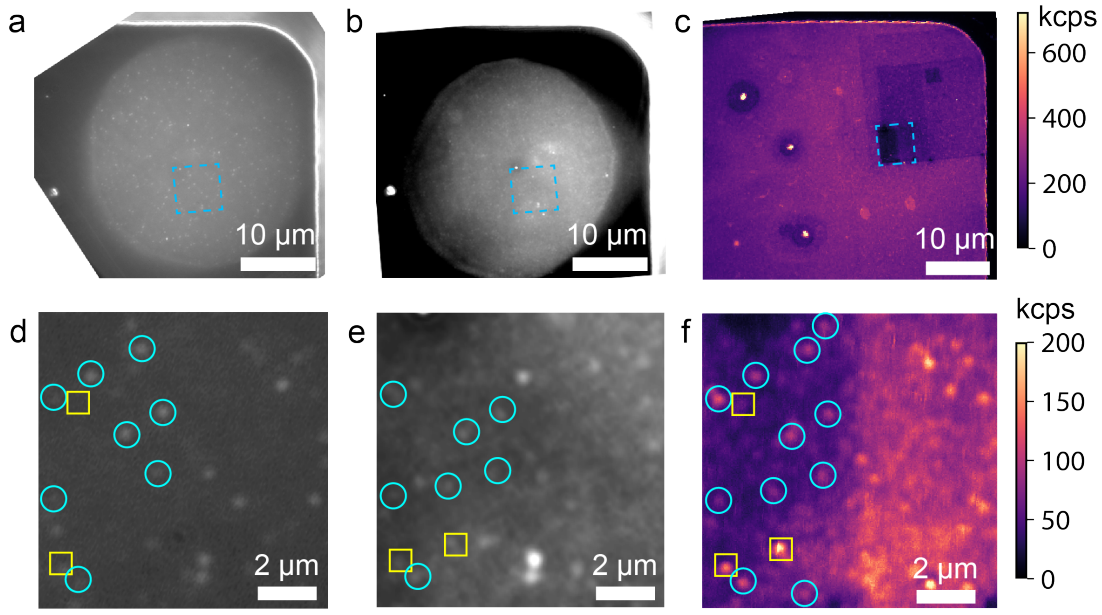

Figure S12: NV^- mapping in widefield and confocal images on Sample A. (a) The widefield image of as-prepared Sample A. This image is the same as Figure 4 (a) in the main text but has been rotated to assist alignment. (b)-(c) The same region of Sample A imaged by (b) widefield and (c) confocal microscopy. Compared to (a), Sample A at the time of acquiring (b) and (c) has been incubated with streptavidin and Qdot-525 and has also been subjected to $4\,\mathrm{K}$ temperature. These treatments alone or combined has increased the fluorescence background, despite of multiple cycles of solvent cleaning. As a consequence, prior to taking image (c) and subsequent ODMR data, we used high laser intensity to scan and bleach certain regions. The bleached regions are cleanly seen as dark rectangle-shaped regions. (d)-(f) The same $10\,\mu\mathrm{m}$ by $10\,\mu\mathrm{m}$ area, indicated by cyan boxes in (a)-(c), are displayed next to each other. In (f), the emitters highlighted by cyan circles are verified NV^- centers with ODMR at $2.87\,\mathrm{GHz}$, while emitters labeled as yellow boxes do not have such ODMR feature. Same symbols are used in (d) and (e) to facilitate visual recognition of the same cluster of emitters via their spatial information (only for the clearly visible ones).

5.3 Surface-tethered molecules on diamond membrane

5.3.1 Biocompatible diamond surface functionalization

The surface functionalization of the bonded diamond membrane was achieved following the strategy introduced in[25], using $3\,\%$ N-[3-(trimethoxysilyl)propyl]ethylenediamine (CAS 1760-24-3, ACROS Organics) in anhydrous acetone for silanization and $0.5\,\mathrm{M}$ PEG-SVA solution (dissolved in $100\,\mathrm{mM}$ $NaHCO_3$, pH 8.5) that comprises $90\,\%$ mPEG-SVA and $10\,\%$ biotinPEG-SVA (m.w. 2,000, Laysan Bio) for PEGylation. After functionalization steps, the diamond membrane surface was displaying biotin motifs that served as specific conjugation sites for streptavidin.

5.3.2 Flow channel assembly

The coverslip was attached to the bottom of an ibidi sticky-Slide VI 0.4 device (Cat.#: 80608) to form a flow channel for subsequent experiments, and the diamond membrane was facing inwards, as shown in Figure S13. Soaking the device in isopropanol overnight can detach the coverslip for recycling.

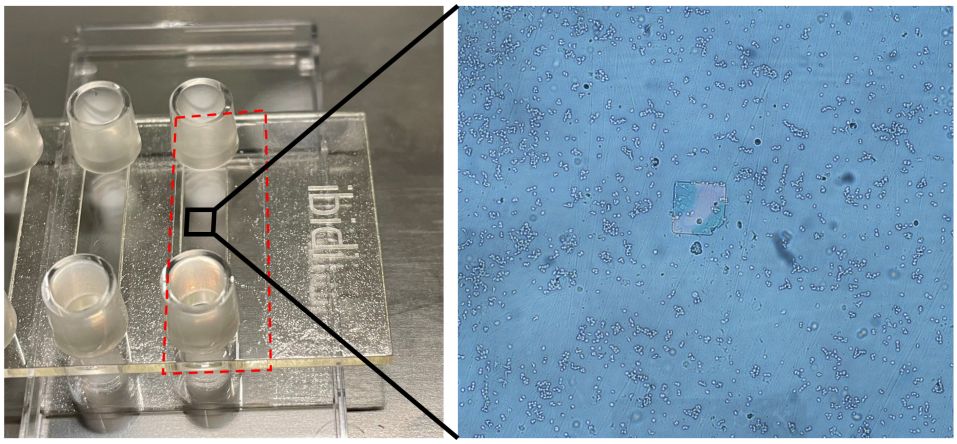

Figure S13: The assembled flow channel device. A fused silica coverslip (red dashed box) with a diamond membrane bonded to the center was attached to a flow channel slide, and RAW cells were incubated, fixed, and stained inside the flow channel, as shown on the right microscopic image.

5.3.3 Incubation and imaging

Attachment of target molecules to the functionalized diamond membrane surface was demonstrated using (1) streptavidin labeled with Alexa-488 dye (Invitrogen Cat#S32354), and (2) streptavidin-conjugated Qdot-525 quantum dots (Invitrogen Cat# Q10143MP). First, $60\,\mu\mathrm{L}$ of $5\,\mathrm{nm}$ dye-labeled streptavidin solution prepared in 1× phosphate buffered saline (PBS) was introduced to the flow channel and incubated for $5\,\mathrm{min}$ at room temperature, before being washed

with 1 mL fresh PBS. Widefield fluorescence microscopy images were taken using 488 nm laser (Coherent Sapphire) illumination and 525/50 nm band-pass imaging filter (Chroma). Once the image acquisition was completed, the same field of view was photobleached for 3 min. Second, 50 µL of 10 nM streptavidin-conjugated Qdot-525 was introduced to the flow channel and incubated for 10 min at room temperature before being washed with 1 mL fresh PBS. The same area was imaged, and the fluorescent spots were predominately Qdot-525 as the Alexa-488 conjugated on streptavidin from the previous round of incubation was already photobleached.

5.3.4 Simultaneous detection of NV^- centers and Qdot-525

Figure S14 (a) shows the dual-color image simultaneously displaying NV^- centers and Qdot-525. This image was acquired by switching the Hamamatsu W-VIEW GEMINI system to dual-imaging mode. The schematics of this mode is shown in Figure S14 (b). Image pairs from the same field of view were separated by wavelength using a ZT532rdc-UF2 (Chroma) dichroic beam splitter, with a 510/20 nm filter (Chroma ET510/20m) in the short wavelength path and a 594 nm long pass filter (Semrock EdgeBasic LP594) in the long wavelength path. During a single exposure which lasted 100 s, 488 nm laser was switched on only for the first 10 s while the 532 nm laser was on for the entire duration to help balance the overall intensities of the two sub-images.

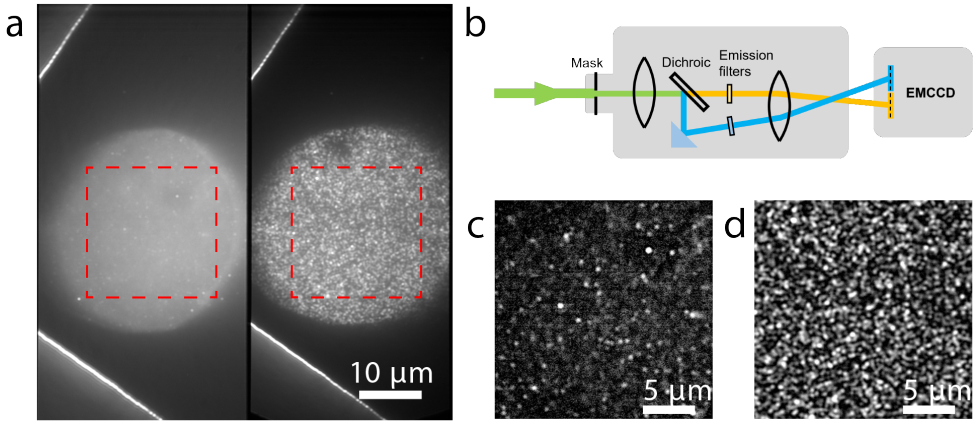

Figure S14: Simultaneous detection of both NV^- and Qdot-525 on Sample A. (a) A single-exposure image acquired on a 1024×1024 pixel EMCCD, showing two sub-images of the same area differentiated by emission wavelengths. The left sub-image shows NV^- and the right one shows Qd-525. (b) Schematic illustration of Hamamatsu W-VIEW GEMINI system. (c)-(d) The zoomed-in view of the regions in (a) indicated by red boxes, respectively. The images were processed in ImageJ to subtract background and improve contrast for visualization. For real-world applications, careful system calibration using fluorescent beads is required for the accurate alignment of the two sub-images to remove small yet systematic distortion. This framework enables the selection of NV^--target molecule pairs that are spatially closed to each other for subsequent quantum sensing experiments.

5.4 RAW cell experiments

We duplicated a new flow channel device for cell culturing. The flow channel was washed with culturing medium (DMEM with $10\,\%$ FBS) and 1×10^5 RAW cells were delivered and incubated at $37\,^{\circ}\mathrm{C}$ and $5\,\%$ CO_2 overnight. The channel was washed with fresh medium and the cells were fixed by incubating with $3\,\%$ of paraformaldehyde for $15\,\mathrm{min}$. The channel was washed again and incubated for $60\,\mathrm{min}$ with 1:100 of $0.5\,\mathrm{mg\,mL^{-1}}$ anti-TLR2 monoclonal antibody (Invitrogen) labeled with Alexa-488 following a standard protocol.[26] Finally, the channel was washed 3 times with PBS for subsequent imaging. Widefield images under $488\,\mathrm{nm}$ laser excitation was acquired by EMCCD with $1\,\mathrm{s}$ exposure time and 300 gain. For each region, the first image was acquired at a very steep TIRF angle, followed by a second image that was acquired under epi-illumination.

5.5 Bacteria experiments

Escherichia coli (*E. coli*, BL21 strain) bacteria that overexpress green fluorescent protein (GFP) were suspended in PBS and introduced to another flow channel. Initially, very few bacteria cells were seen to settle on the diamond membrane surface using fluorescence microscopy. After approximately $6\,\mathrm{h}$ of sediment, a much higher density of cells was observed on the diamond membrane surface and images/videos were taken with $488\,\mathrm{nm}$ laser illumination under this condition. See Supplementary Video S1 as an example.

5.6 TIRF condition and evanescent field profile

The depth resolution of TIRF microscopy originates from the rapid evanescent field decay of light incident at angles greater than the critical angle. The critical angle of our system, referenced in glass, is $\theta_c = sin^{-1}(n_{water}/n_{glass}) \approx 66°$. We used finite difference time domain simulations (Lumerical, FDTD) to calculate the electric intensity profile across the diamond membrane stack. Figure S15 (a) is an illustrative plot of the normalized electric field intensity for p-polarized light, incident at an angle of $70°$ on a $160\,\mathrm{nm}$-thick diamond membrane; the field decays exponentially into the water layer. Figure S15 (b) is a plot of the extracted decay constant in the water layer computed from both FDTD and the analytic expression $\frac{\lambda_0}{4\pi}(n_1^2 sin^2(\theta) - n_2^2)^{-1/2}$ for incident angles greater than θ_c. Such large incident angles are accessible in our setup due to the 1.5 N.A. of the oil-immersion objective. From this analysis, we expect our diamond-membrane TIRF configuration to have depth resolution $\leq 100\,\mathrm{nm}$.

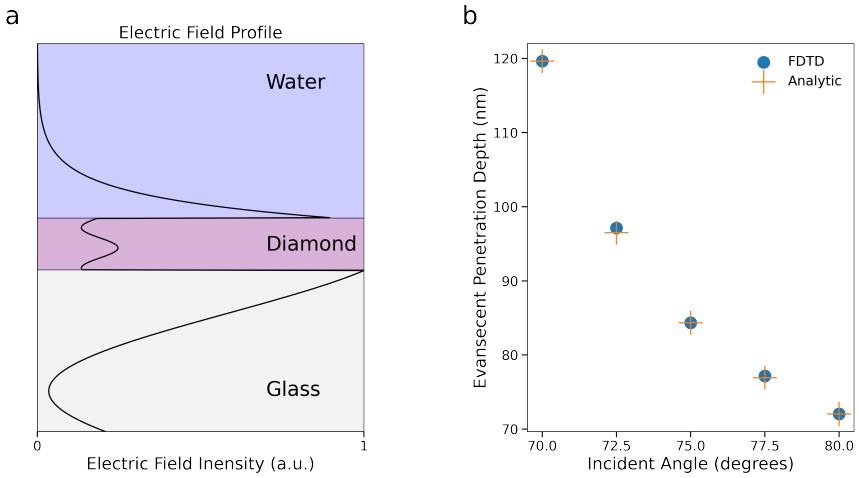

Figure S15: Calculated intensity profile in diamond-membrane TIRF microscopy. (a) FDTD-calculated electric field intensity profile across a $160\,\mathrm{nm}$-thick diamond membrane between a glass substrate and water. Here, the light is p-polarized and incident at an angle of $70°$, as referenced in the glass substrate. (b) Intensity decay constant in the water layer calculated using FDTD (blue circle) and analytically (orange cross) for angles greater than the critical angle.

5.7 Spin coherence of NV$^-$ centers in direct-bonded membranes

The spin coherence of NV$^-$ centers is critical to their performance as nanoscale quantum sensors. In a previous study[1], we have experimentally measured technology-compatible room temperature spin coherence of individual NV$^-$ centers in diamond membranes, reflecting the pristine crystal quality and atomically smooth surfaces of the membrane. In this section, we investigate the impact of the direct bonding process on NV$^-$ coherence to determine if the processes introduce additional decoherence processes. The device consists of a $150\,\mathrm{nm}$-thick diamond membrane bonded to a thermal oxide wafer. The membrane contains implanted and naturally formed ^{14}NV$^-$ centers, as well as naturally formed ^{15}NV$^-$ centers. The existence of background ^{15}NV$^-$ originates from the diamond growth chamber which is regularly used for δ-doping of [^{15}N]. Measurements are performed at room temperature, with the microwave drive introduced via a coplanar waveguide patterned onto a glass coverslip, as shown in Figure S16 (g). Two NV$^-$ centers were randomly chosen and characterized, one with an intrinsic [^{15}N] while the other with [^{14}N]. Both centers were identified via the ODMR features shown in Figure S16 (a)-(b). The Ramsey measurement shown in Figure S16 (c)-(d) shows T_2^* of $92(16)\,\mu\mathrm{s}$ and $66(9)\,\mu\mathrm{s}$, respectively. The Fourier transform of T_2^* measurements with a much finer scan (to avoid undersampling) are shown in Figure S16 (e)-(f). We note that the ^{15}NV$^-$ (Figure S16 (e)) is coupled to a nearby ^{13}C nuclear spin, which results in an oscillation pattern in the spin echo measurement, as shown in Figure 2 (g) of the main text with a Hahn echo T_2 of $632(21)\,\mu\mathrm{s}$ (T_2 fitting superscript $n = 1.35 \pm 0.04$). The fitting details of Hahn echo T_2 is described below.

We first analyze the interaction term from the weakly coupled ^{13}C. In the rotational frame of the NV$^-$ electron spin the Hamiltonian is given by:

$$\mathcal{H} = \omega_n I_z + S_z(AI_z + BI_x) = (Am_s - \omega_n)Iz + Bm_s I_x \tag{1}$$

Where $m_s \in \{0, 1\}$ is determined by the electron spin state. Diagonalizing the Hamiltonian gives the resonance frequency $K = \sqrt{(Am_s - \omega_n)^2 + (Bm_s)^2}$, such that
$K_+ = \sqrt{(A - \omega_n)^2 + (B)^2}$ and $K_- = \omega_n$. The fitting function can thus be simplified to the following form:

$$\begin{aligned} f(\tau) &= Ae^{(-\frac{\tau}{T_2})^n}\left[1 + 2\left(\frac{B\omega_n}{K_+K_-}\right)^2 \sin^2\left(\frac{2\pi K_+\tau}{4} + \phi_0\right)\sin^2\left(\frac{2\pi K_-\tau}{4} + \phi_1\right)\right] \\ &= Ae^{(-\frac{\tau}{T_2})^n}\left[1 + 2\left(\frac{B}{K_+}\right)^2 \sin^2\left(\frac{2\pi K_+\tau}{4} + \phi_0\right)\sin^2\left(\frac{2\pi K_-\tau}{4} + \phi_1\right)\right] \end{aligned} \tag{2}$$

Notice that τ in our case is defined to be the time from the beginning of the first $\frac{\pi}{2}$ pulse to the end of the last $\frac{\pi}{2}$, as such there is an additional factor of 2 compared to the formula from the original paper.[27]
The modulation frequencies—$97.32(5)\,\mathrm{kHz}$ and $14.82(5)\,\mathrm{kHz}$—correspond respectively to the free precession of ^{13}C at $\sim$ 91 Gauss (the magnetic field used for spin measurements) and the combination of free precession and coherent coupling strength of the ^{13}C to the ^{15}NV$^-$. Fitting our spin echo data returns $B = 13.14(14)\,\mathrm{kHz}$. From our derivation above, we obtain $A = \omega_n \pm \sqrt{K_+^2 - B^2}$, which is $90.493\,\mathrm{kHz}$ or $104.176\,\mathrm{kHz}$. We can make a rough estimate of the separation between the ^{13}C and our NV center by ignoring the Fermi contact interaction. This can be done as follows:

$$\begin{aligned} A &= \frac{\mu_0\gamma_e\gamma_n\hbar}{4\pi r^3}(3cos(\theta)^2 - 1) \\ B &= \frac{\mu_0\gamma_e\gamma_n\hbar}{4\pi r^3}3cos(\theta)sin(\theta) \end{aligned} \tag{3}$$

Solving for θ and r gives:[28]

$$\begin{aligned} \theta &= \arctan\left(\frac{1}{2}\left(-3\frac{A}{B} + \sqrt{9\frac{A^2}{B^2} + 8}\right)\right) \\ r &= \left(\frac{\mu_0\gamma_e\gamma_n\hbar(3\cos^2(\theta) - 1)}{4\pi A}\right)^{1/3} \end{aligned} \tag{4}$$

We then have $r = 1.40\,\mathrm{nm}$ with $\theta = 5.5^\circ$ or $r = 1.33\,\mathrm{nm}$ with $\theta = 4.8^\circ$ corresponding to $A = 90.493$ or $104.176\,\mathrm{kHz}$.
In Figure 2 (g) of the main text, a well-aligned magnetic field along the NV$^-$ axis suppresses the ^{15}N modulation on the spin echo signal. In contrast, in Figure S16 (h) ^{14}NV$^-$'s large quadrupole

interaction at low magnetic fields suppresses modulation regardless of magnetic field alignment[29]. Therefore, it returns a simple decay without modulation and a corresponding Hahn echo T_2 of $278(13)$ µs (T_2 fitting superscript $n = 1.30 \pm 0.06$). We note that the coherence time is comparable to the NV^- centers' value measured at the suspended region[1], indicating negligible added noise from the direct bonding process. The distribution of T_2 is affected by the depth of NV^- centers as discussed in Ref.[30], and this effect becomes more apparent in our diamond membrane system where two surfaces are present. In the future, a more rigorous characterization regarding optical and spin coherence of NV^- centers in ultra-shallow diamond membranes will be conducted, which is beyond the scope of the current work.

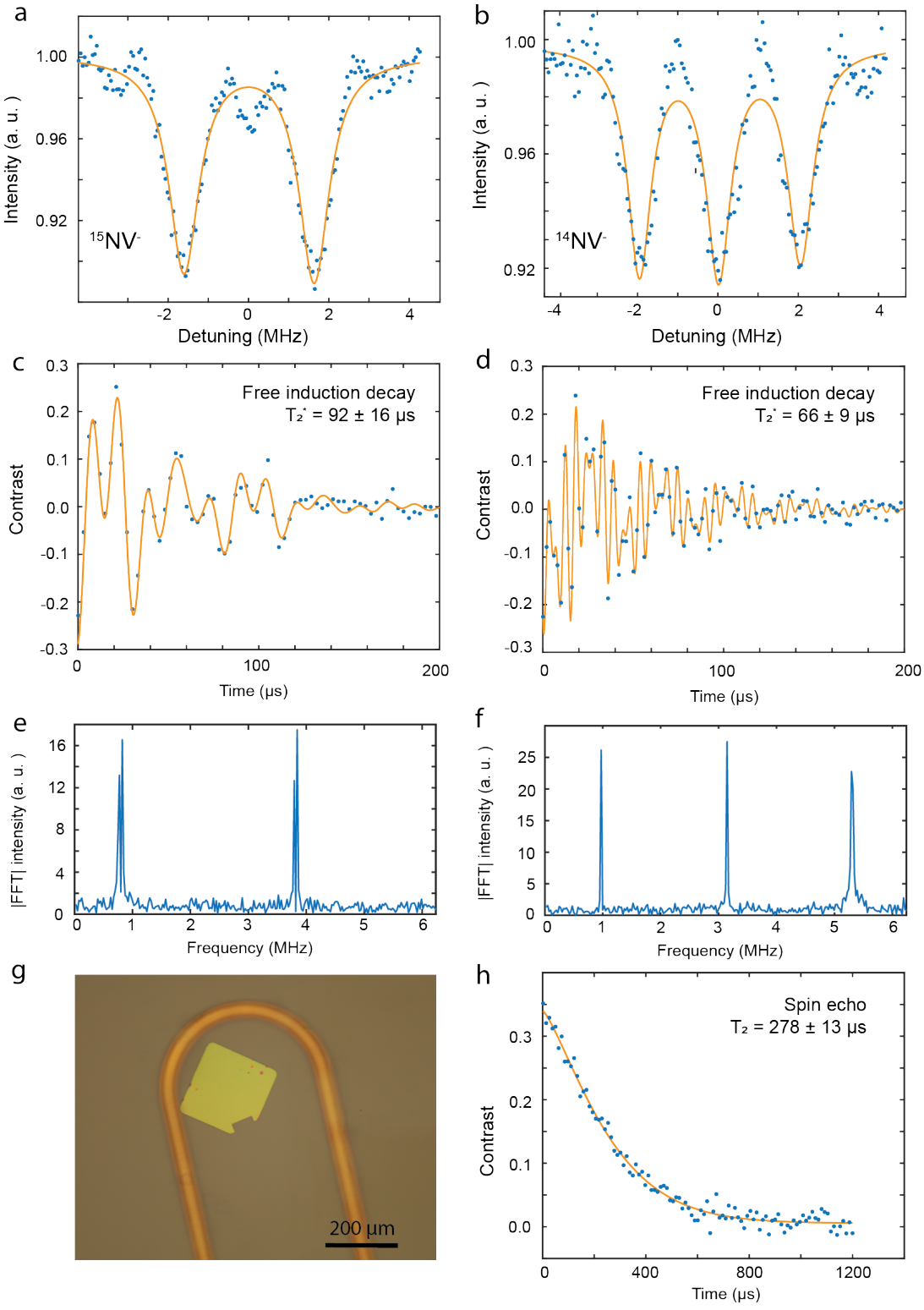
a
Intensity (a. u.)
1.00
0.96
0.92
$^{15}NV^-$
-2
0
2
4
Detuning (MHz)
b
Intensity (a. u.)
1.00
0.96
0.92
$^{14}NV^-$
-4
-2
0
2
4
Detuning (MHz)
c
Contrast
Free induction decay
$T_2^* = 92 \pm 16$ µs
0.3
0.2
0.1
0.0
-0.1
-0.2
-0.3
0
100
200
Time (µs)
d
Contrast
Free induction decay
$T_2^* = 66 \pm 9$ µs
0.3
0.2
0.1
0.0
-0.1
-0.2
-0.3
0
100
200
Time (µs)
e
|FFT| intensity (a. u.)
16
12
8
4
0
0
1
2
3
4
5
6
Frequency (MHz)
f
|FFT| intensity (a. u.)
25
20
15
10
5
0
0
1
2
3
4
5
6
Frequency (MHz)
g
200 µm
h
Contrast
Spin echo
$T_2 = 278 \pm 13$ µs
0.3
0.2
0.1
0.0
0
400
800
1200
Time (µs)

Figure S16: Typical spin coherence of NV centers in direct-bonded membranes at room temperature. (a), (c), (e) were measured on a single $^{15}NV^-$ while (b), (d), (f), (h) were measured on a single $^{14}NV^-$. (a)-(b): the ODMR spectra. We simplified the fitting using multi-peak Lorentzian to retrieve the ODMR frequency and linewidth. A more careful fitting with multiple Rabi formula curves could lead to a more precise fit. (c)-(d): Free induction decay (Ramsey measurement) of the NV^-s. Both NV^-s show notably long T_2^* times due to the isotopic purification during overgrowth. (e)-(f): Fourier transformations of finely sampled Ramsey measurements show the Larmor precession frequencies coming from in e) the intrinsic ^{15}N with additional splitting from a distant ^{13}C and in (f) only the intrinsic ^{14}N. (g) A bright-field microscope image of the Ω-shape coplanar waveguide used for microwave signal delivery to the diamond membrane. (h) Hahn echo measurements of the $^{14}NV^-$ showing a long T_2 value with a simple decay.

6 Additional XPS figures

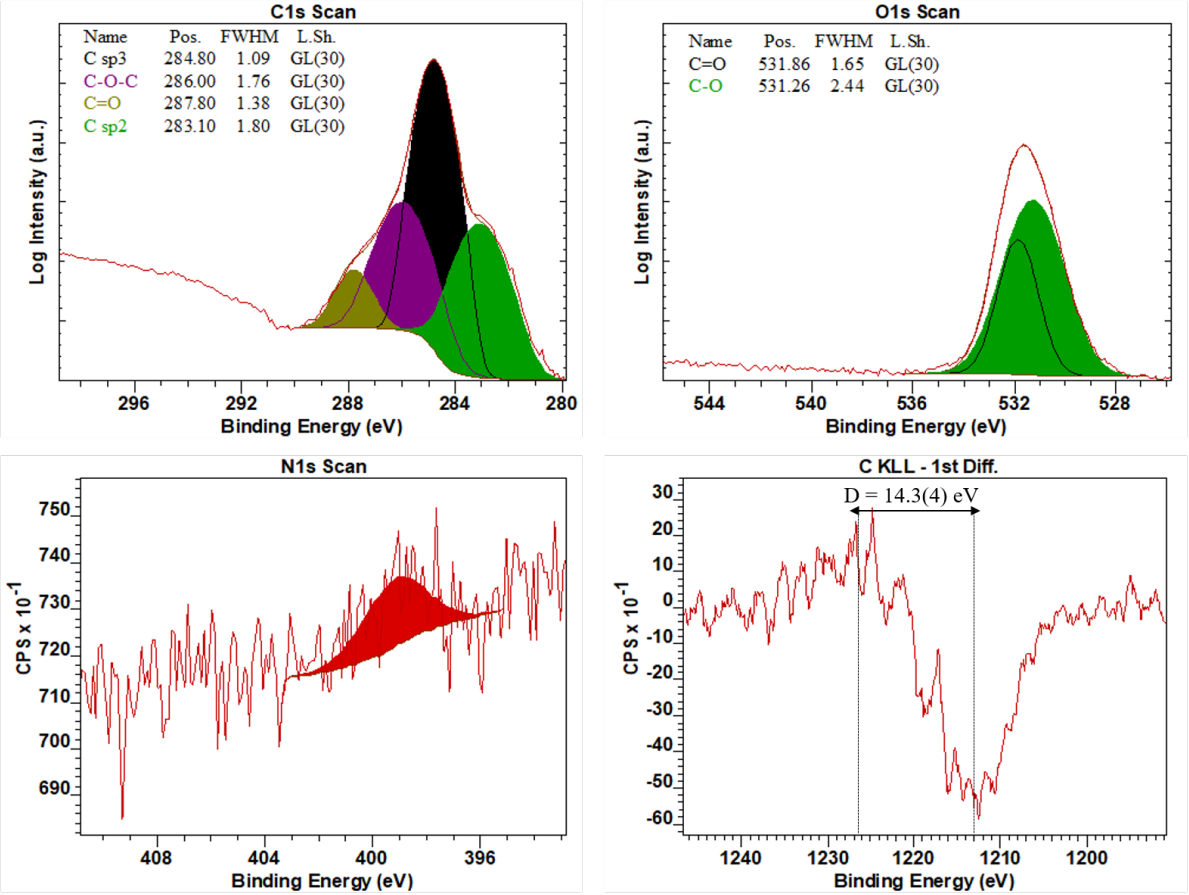

Figure S17: XPS characterization of the processed diamond substrate, showing the C 1s and O 1s deconvolutions with component labels and fitting parameters. sp^2 content quantification is achieved via D parameter linear extrapolation of the C KLL first order derivative[12,13]. N 1s peak contamination also showed as samples were exposed to atmosphere. Some of the peak fittings are presented in log scale to help discern minority components.

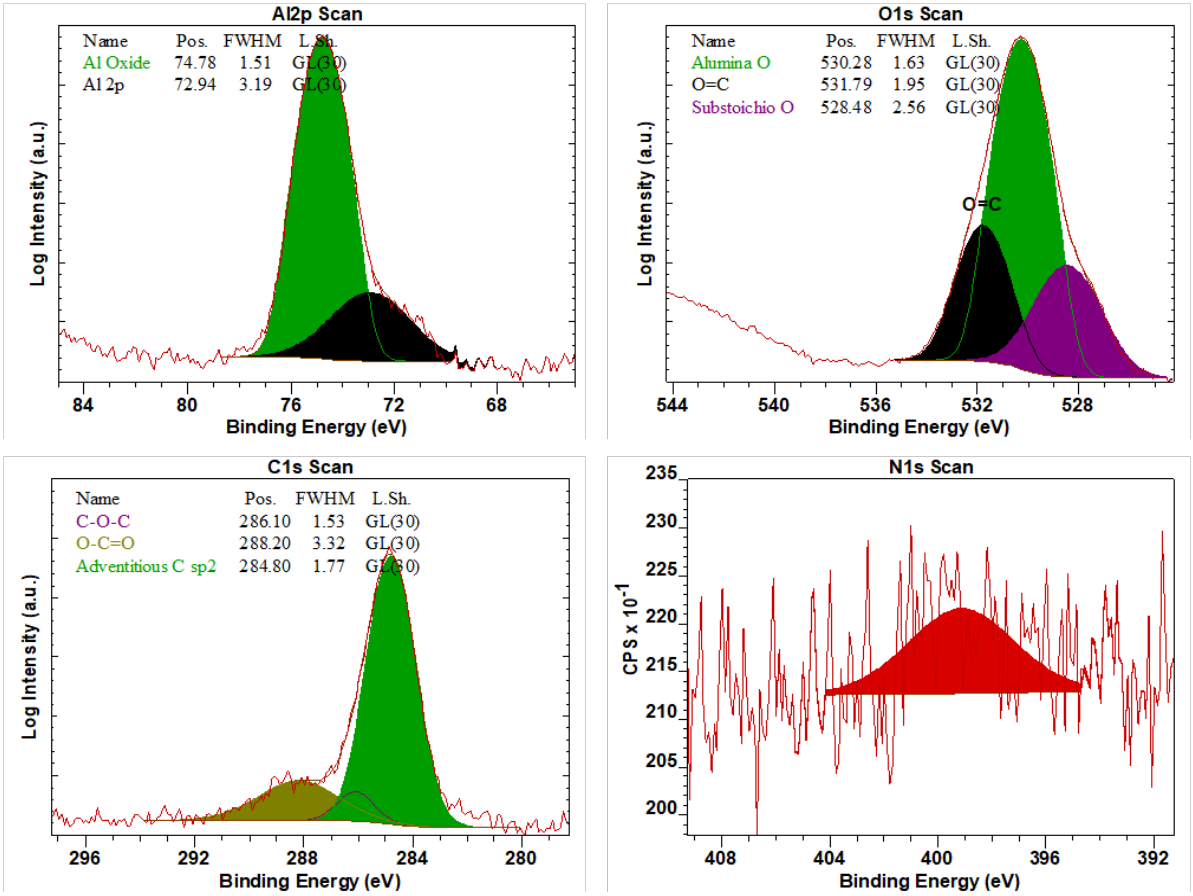

Figure S18: XPS characterization of the unprocessed sapphire substrate, showing the Al 2p, O 1s, and C 1s deconvolutions with component labels and fitting parameters. N 1s peak contamination also showed as samples were exposed to atmosphere. Some of the peak fittings are presented in log scale to help discern minority components.

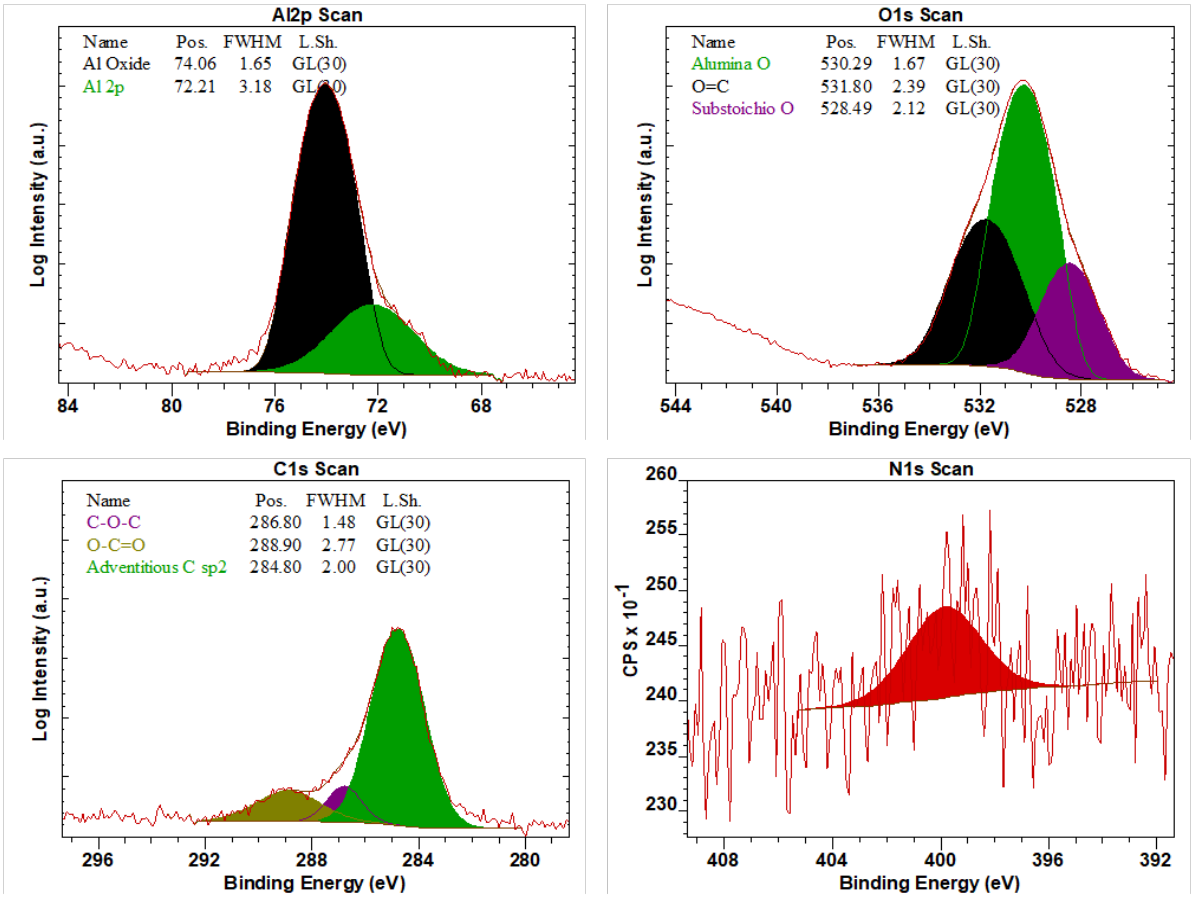

Figure S19: XPS characterization of the processed sapphire substrate, showing the Al 2p, O 1s, and C 1s deconvolutions with component labels and fitting parameters. N 1s peak contamination also showed as samples were exposed to atmosphere. Some of the peak fittings are presented in log scale to help discern minority components.

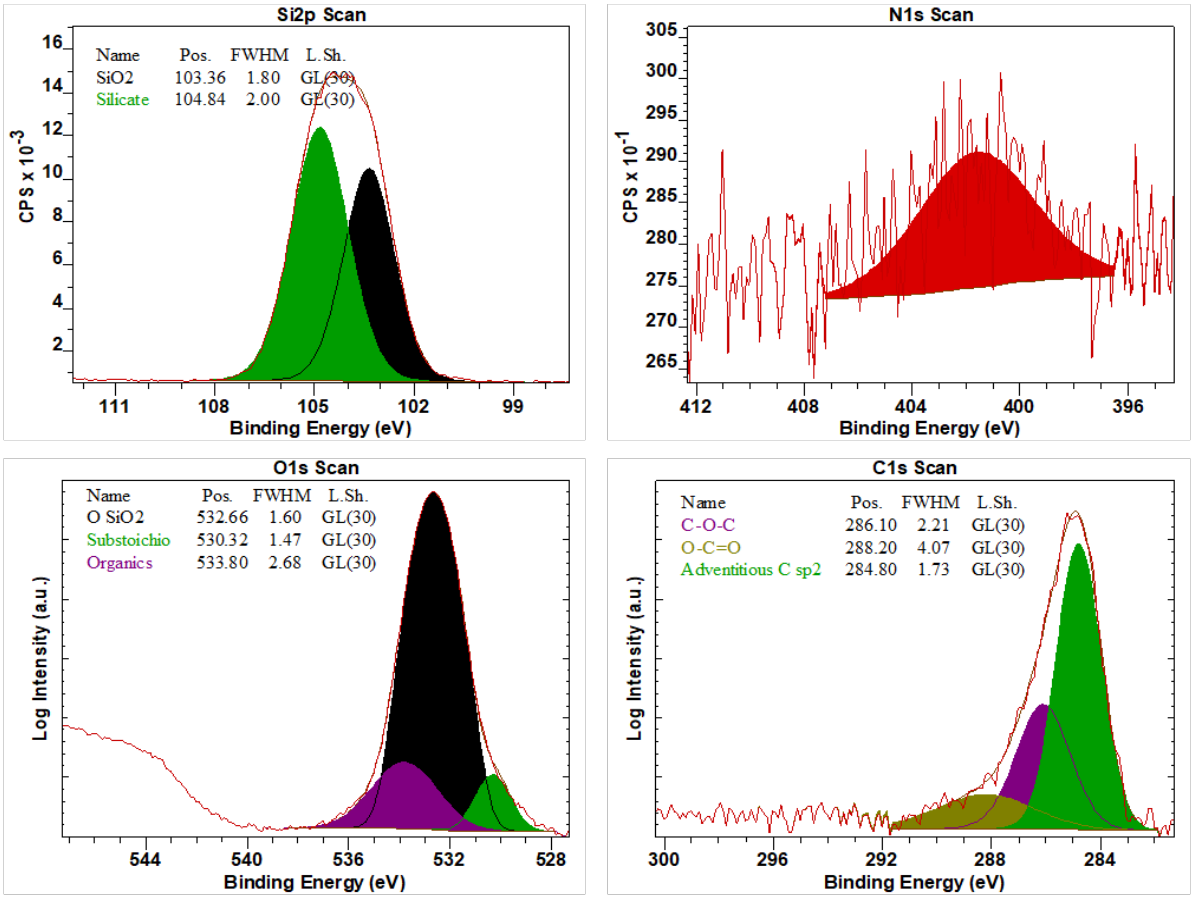

Figure S20: XPS characterization of the unprocessed sapphire substrate, showing the Si 2p, O 1s, and C 1s deconvolutions with component labels and fitting parameters. N 1s peak contamination also showed as samples were exposed to atmosphere. Some of the peak fittings are presented in log scale to help discern minority components.

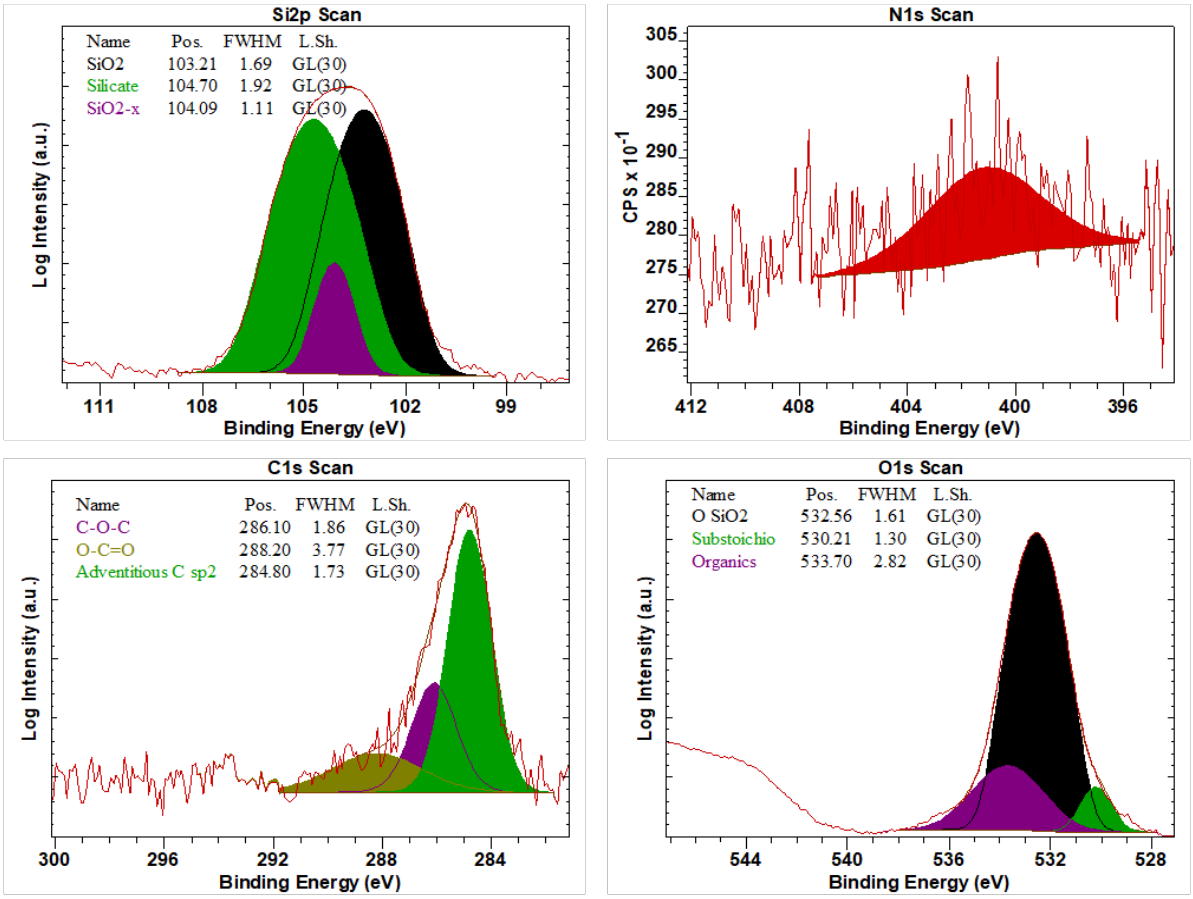

Figure S21: XPS characterization of the processed sapphire substrate, showing the Si 2p, O 1s, and C 1s deconvolutions with component labels and fitting parameters. N 1s peak contamination also showed as samples were exposed to atmosphere. Some of the peak fittings are presented in log scale to help discern minority components.

References

[1] X. Guo, N. Delegan, J. C. Karsch, Z. Li, T. Liu, R. Shreiner, A. Butcher, D. D. Awschalom, F. J. Heremans, A. A. High, Tunable and transferable diamond membranes for integrated quantum technologies, *Nano Letters* **2021**, *21* 10392.

[2] R. Huang, T. Lan, C. Li, Z. Wang, Plasma-activated direct bonding at room temperature to achieve the integration of single-crystalline gaas and si substrate, *Results in Physics* **2021**, *31* 105070.

[3] L. Pasternak, Y. Paz, Low-temperature direct bonding of silicon nitride to glass, *RSC Adv.* **2018**, *8* 2161.

[4] F. Wang, X. Yang, Y. Zhao, J. Wu, Z. Guo, Z. He, Z. Fan, F. Yang, Low-temperature direct bonding of sic to si via plasma activation, *Applied Sciences* **2022**, *12*, 7.

[5] S. Sangtawesin, B. L. Dwyer, S. Srinivasan, J. J. Allred, L. V. Rodgers, K. De Greve, A. Stacey, N. Dontschuk, K. M. O'Donnell, D. Hu, D. A. Evans, C. Jaye, D. A. Fischer, M. L. Markham, D. J. Twitchen, H. Park, M. D. Lukin, N. P. de Leon, Origins of Diamond Surface Noise Probed by Correlating Single-Spin Measurements with Surface Spectroscopy, *Physical Review X* **2019**, *9*, 3 31052.

[6] B. Zhuang, S. Li, S. Li, J. Yin, Ways to eliminate pmma residues on graphene —— superclean graphene, *Carbon* **2021**, *173* 609.

[7] N. H. Wan, T.-J. Lu, K. C. Chen, M. P. Walsh, M. E. Trusheim, L. De Santis, E. A. Bersin, I. B. Harris, S. L. Mouradian, I. R. Christen, E. S. Bielejec, D. Englund, Large-scale integration of artificial atoms in hybrid photonic circuits, *Nature* **2020**, *583*, 7815 226.

[8] M. Ruf, M. Ijspeert, S. Van Dam, N. De Jong, H. Van Den Berg, G. Evers, R. Hanson, Optically Coherent Nitrogen-Vacancy Centers in Micrometer-Thin Etched Diamond Membranes, *Nano Letters* **2019**, *19*, 6 3987.

[9] J. C. Lee, A. P. Magyar, D. O. Bracher, I. Aharonovich, E. L. Hu, Fabrication of thin diamond membranes for photonic applications, *Diamond and Related Materials* **2013**, *33* 45.

[10] A. Tallaire, M. Kasu, K. Ueda, T. Makimoto, Origin of growth defects in CVD diamond epitaxial films, *Diamond and Related Materials* **2008**, *17*, 1 60.

[11] C. Y. Yeo, D. W. Xu, S. F. Yoon, E. A. Fitzgerald, Low temperature direct wafer bonding of GaAs to Si via plasma activation, *Applied Physics Letters* **2013**, *102*, 5, 054107.

[12] B. Lesiak, L. Kövér, J. Tóth, J. Zemek, P. Jiricek, A. Kromka, N. Rangam, C sp2/sp3 hybridisations in carbon nanomaterials – XPS and (X)AES study, *Applied Surface Science* **2018**, *452* 223.

[13] A. Mezzi, S. Kaciulis, Surface investigation of carbon films: from diamond to graphite, *Surface and Interface Analysis* **2010**, *42*, 6-7 1082.

[14] Nist x-ray photoelectron spectroscopy database, https://srdata.nist.gov/xps/, URL https://srdata.nist.gov/xps/.

[15] X. Guo, A. M. Stramma, Z. Li, W. G. Roth, B. Huang, Y. Jin, R. A. Parker, J. Arjona Martínez, N. Shofer, C. P. Michaels, C. P. Purser, M. H. Appel, E. M. Alexeev, T. Liu, A. C. Ferrari, D. D. Awschalom, N. Delegan, B. Pingault, G. Galli, F. J. Heremans, M. Atatüre, A. A. High, Microwave-based quantum control and coherence protection of tin-vacancy spin qubits in a strain-tuned diamond-membrane heterostructure, *Phys. Rev. X* **2023**, *13* 041037.

[16] S. Meesala, Y.-I. Sohn, B. Pingault, L. Shao, H. A. Atikian, J. Holzgrafe, M. Gündoğan, C. Stavrakas, A. Sipahigil, C. Chia, R. Evans, M. J. Burek, M. Zhang, L. Wu, J. L. Pacheco, J. Abraham, E. Bielejec, M. D. Lukin, M. Atatüre, M. Lončar, Strain engineering of the silicon-vacancy center in diamond, *Physical Review B* **2018**, *97*, 20 205444.

[17] M. K. Bhaskar, D. D. Sukachev, A. Sipahigil, R. E. Evans, M. J. Burek, C. T. Nguyen, L. J. Rogers, P. Siyushev, M. H. Metsch, H. Park, F. Jelezko, M. Lončar, M. D. Lukin, Quantum nonlinear optics with a germanium-vacancy color center in a nanoscale diamond waveguide, *Phys. Rev. Lett.* **2017**, *118* 223603.

[18] Z. H. Zhang, J. A. Zuber, L. V. Rodgers, X. Gui, P. Stevenson, M. Li, M. Batzer, M. L. G. Puigibert, B. J. Shields, A. M. Edmonds, N. Palmer, M. L. Markham, R. J. Cava, P. Maletinsky, N. P. D. Leon, Neutral silicon vacancy centers in undoped diamond via surface control, *Physical Review Letters* **2023**, *13*.

[19] C. Schreyvogel, V. Polyakov, R. Wunderlich, J. Meijer, C. E. Nebel, Active charge state control of single nv centres in diamond by in-plane al-schottky junctions, *Scientific Reports* **2015**, *5* 12160.

[20] M. Salvadori, W. Araújo, F. Teixeira, M. Cattani, A. Pasquarelli, E. Oks, I. Brown, Termination of diamond surfaces with hydrogen, oxygen and fluorine using a small, simple plasma gun, *Diamond and Related Materials* **2010**, *19*, 4 324.

[21] E. Janitz, K. Herb, L. A. Völker, W. S. Huxter, C. L. Degen, J. M. Abendroth, Diamond surface engineering for molecular sensing with nitrogen—vacancy centers, *Journal of Materials Chemistry C* **2022**, *10*, 37 13533.

[22] C. Macklin, UC Berkeley UC Berkeley Electronic Theses and Dissertations, *DNA Mediated Assembly of Protein Heterodimers on Membrane Surfaces* **2020**, 67.

[23] A. Butcher, X. Guo, R. Shreiner, N. Delegan, K. Hao, P. J. Duda, D. D. Awschalom, F. J. Heremans, A. A. High, High-Q Nanophotonic Resonators on Diamond Membranes using Templated Atomic Layer Deposition of TiO2, *Nano Letters* **2020**, *20*, 6 4603.

[24] G. M. Hasan, P. Liu, M. Hasan, H. Ghorbani, M. Rad, E. Bernier, T. J. Hall, Ring resonator gap determination design rule and parameter extraction method for sub-ghz resolution whole c-band si3n4 integrated spectrometer, *Photonics* **2022**, *9*, 9.

[25] M. Xie, X. Yu, L. V. H. Rodgers, D. Xu, I. Chi-Durán, A. Toros, N. Quack, N. P. de Leon, P. C. Maurer, Biocompatible surface functionalization architecture for a diamond quantum sensor, *Proceedings of the National Academy of Sciences* **2022**, *119*, 8 e2114186119.

[26] Alexa fluor ® 488 microscale protein labeling kit (a30006), https://www.thermofisher.com/document-connect/document-connect.html?url=https://assets.thermofisher.com/TFS-Assets%2FLSG%2Fmanuals%2Fmp30006.pdf, URL https://www.thermofisher.com/document-connect/document-connect.html?url=https://assets.thermofisher.com/TFS-Assets%2FLSG%2Fmanuals%2Fmp30006.pdf.

[27] L. G. Rowan, E. L. Hahn, W. B. Mims, Electron-spin-echo envelope modulation, *Phys. Rev.* **1965**, *137* A61.

[28] J. M. Boss, K. Chang, J. Armijo, K. Cujia, T. Rosskopf, J. R. Maze, C. L. Degen, One- and two-dimensional nuclear magnetic resonance spectroscopy with a diamond quantum sensor, *Phys. Rev. Lett.* **2016**, *116* 197601.

[29] L. Childress, M. V. G. Dutt, J. M. Taylor, A. S. Zibrov, F. Jelezko, J. Wrachtrup, P. R. Hemmer, M. D. Lukin, Coherent dynamics of coupled electron and nuclear spin qubits in diamond, *Science* **2006**, *314*, 5797 281.

[30] K. Ohno, F. Joseph Heremans, L. C. Bassett, B. A. Myers, D. M. Toyli, A. C. Bleszynski Jayich, C. J. Palmstrøm, D. D. Awschalom, Engineering shallow spins in diamond with nitrogen delta-doping, *Applied Physics Letters* **2012**, *101*, 8 082413.